Clim Dyn (2016) 46:205–226
DOI 10.1007/s00382-015-2579-0

A study of biases in simulation of the Indian Ocean basin mode and its capacitor effect in CMIP3/CMIP5 models

Weichen Tao[1,6] · Gang Huang[1,2] · Kaiming Hu[1,2,3] · Hainan Gong[3,6] · Guanhuan Wen[4] · Lin Liu[5]

Received: 9 October 2014 / Accepted: 24 March 2015 / Published online: 8 April 2015

Abstract Based on 15 Coupled Model Intercomparison Project (CMIP) phase 3 (CMIP3) and 32 CMIP phase 5 (CMIP5) models, a detailed diagnosis was carried out to understand what compose the biases in simulation of the Indian Ocean basin mode (IOBM) and its capacitor effect. Cloud-radiation-SST (CRS) feedback and wind-evaporation-SST (WES) feedback are the two major atmospheric processes for SST changes. Most CMIP models simulate a stronger CRS feedback and a weaker WES feedback. During boreal fall of the El Niño/Southern Oscillation developing year and the following spring, there are weak biases of suppressed rainfall anomalies over the Maritime Continent and anomalous anticyclone over South Indian Ocean. Most CMIP models simulate reasonable short wave radiation (SWR) and weaker latent heat flux (LHF) anomalies. This leads to a weak bias of atmospheric processes. During winter, however, the rainfall anomalies are stronger due to west bias, and the anomalous anticyclone is comparable to observations. As such, most models simulate stronger SWR and reasonable LHF anomalies, leading to a strong bias of atmospheric processes. The thermocline feedback is stronger in most models. Though there is a deep bias of climatology thermocline, most models capture reasonable sea surface height-induced SST anomalies. Therefore, the effect of oceanic processes offset the weak bias of atmospheric processes in spring, and the tropical Indian Ocean warming persists into summer. However, anomalous northwest Pacific (NWP) anticyclone is weaker due to weak and west bias of the capacitor effect. The unrealistic western Pacific SST anomalies in models favor the westward extension of Rossby wave from the Pacific, weakening the effect of Kelvin wave from the Indian Ocean. Moreover, the western Pacific warming forces the NWP anticyclone move farther north than observations, suggesting a major forcing from the Pacific. Compared to CMIP3, CMIP5 models simulate the feedbacks more realistically and display less diversity. Thus, the overall performance of CMIP5 models is better than that of CMIP3 models.

Keywords CMIP models · IOBM · Atmospheric and oceanic processes · The capacitor effect · Model biases

✉ Gang Huang
hg@mail.iap.ac.cn

[1] State Key Laboratory of Numerical Modeling for Atmospheric Sciences and Geophysical Fluid Dynamics,Institute of Atmospheric Physics, Chinese Academy of Sciences, 100029 Beijing, China

[2] Joint Center for Global Change Studies, 100875 Beijing, China

[3] Center for Monsoon System Research, Institute of Atmospheric Physics, Chinese Academy of Sciences, 100029 Beijing, China

[4] Guangzhou Institute of Tropical and Marine Meteorology/ Guangdong Provincial Key Laboratory of RegionalNumerical Weather Prediction, China Meteorological Administration, 510080 Guangzhou, China

[5] Center for Ocean and Climate Research, First Institute of Oceanography, State Oceanic Administration, 266061 Qingdao, China

[6] University of Chinese Academy of Sciences, 100049 Beijing, China

1 Introduction

The first leading mode of the interannual Indian Ocean SST variability features a basin-wide warming or cooling, called as the Indian Ocean Basin Mode (IOBM; Yulaeva and Wallace 1994; Klein et al. 1999; Alexander et al.

2002; Chowdary and Gnanaseelan 2007; Yang et al. 2007; Du et al. 2009; Schott et al. 2009; Tao et al. 2014). During the summer when El Niño has dissipated, the IOBM warming can trigger a Matsuno-Gill (Matsuno 1966; Gill 1980) response with warm tropospheric Kelvin wave to east, which contribute to the development of an anomalous northwest Pacific (NWP) anticyclone via the "capacitor effect" (Yang et al. 2007, 2010; Xie et al. 2009), the meridional displacement of the East Asian jet (Qu and Huang 2012b) and the intensification of the South Asia high (Huang et al. 2011; Qu and Huang 2012a). Thus, the IOBM has a strong impact on the East Asian climate, including summer rainfall (Xie et al. 2010), typhoon (Du et al. 2011), high temperature extremes (Hu et al. 2011, 2012a, b) and so on.

IOBM generally develops during boreal winter when El Niño/Southern Oscillation (ENSO) matures, reaches its peak in the following spring (Alexander et al. 2002; Lau and Nath 2003; Schott et al. 2009), and persists into summer (Du et al. 2009). Numerous studies have investigated mechanisms for the IOBM formation. Lau and Nath (1996) showed that El Niño-induced anomalous atmospheric circulation can explain the IOBM warming through reducing surface evaporation and increasing downward short wave radiation, which is known as "atmospheric bridge" mechanism. The spread of tropospheric temperature (TT) anomalies from the eastern Pacific to the remote tropics is an important process in such atmospheric bridge, which is called TT mechanism (Chiang and Sobel 2002; Chiang and Lintner 2005). Klein et al. (1999) reported that surface net heat flux (NHF) anomalies can explain most of the tropical Indian Ocean (TIO) warming, but the tropical southwest Indian Ocean (SWIO) is an exception, where ocean dynamics is important (Lau and Nath 2000). During the developing and mature phases of El Niño, anticyclonic wind anomalies over the South Indian Ocean (SIO) force downwelling Rossby waves (Masumoto and Meyers 1998). The westward Rossby wave is responsible for the SST rise in the SWIO because of shallow mean thermocline there (Xie et al. 2002). After the warming of SWIO, the SST anomalies strengthen the atmospheric convection there in boreal spring (Xie et al. 2002; Du et al. 2009). The intensified convection excites an equatorially antisymmetric pattern of wind anomalies (Wu et al. 2008) as a key to the IOBM persisting into boreal summer by reducing prevailing southwesterly winds over the North Indian Ocean (Du et al. 2009).

Therefore, IOBM is not simply a passive response to ENSO, and there are complex air-sea interactions in the evolution of IOBM and its influence to remote regions. It is a challenge for the coupled ocean–atmosphere general circulation models (CGCMs) to simulate realistically the IOBM. The World Climate Research Programme's (WCRP's) Coupled Model Intercomparison Project (CMIP) phase 3 and phase 5 (CMIP3 and CMIP5) for Fourth and Fifth Assessment Report (AR4 and AR5; Meehl et al. 2007; Taylor et al. 2011) provide good opportunities to explore IOBM and its capacitor effect using state-of-the-art CGCMs. Most of the CMIP models reproduce the IOBM pattern (Saji et al. 2006; Du et al. 2013). In an analysis of CMIP3 models, Saji et al. (2006) found that the simulation of IOBM is highly associated with the simulation of ENSO. Subsequent study with the CMIP5 models displayed the characteristics of local air-sea interactions within the basin in models, and found that half of these models capture the key processes over the Indian Ocean (Du et al. 2013). The interdecadal changes in the ENSO-IOBM and ENSO-NWP anticyclone relationship are investigated in two recent studies (Hu et al. 2014; Tao et al. 2015). Their results showed that IOBM and its capacitor effect strengthen under global warming, which is first mentioned by analyzing the GFDL CM2.1 simulation (Zheng et al. 2011).

Previous studies have formed the basis for further in-depth studies of ENSO teleconnections and local air-sea interactions in TIO. It is necessary to investigate the biases of processes in the evolution of IOBM. Besides, there is still no research on the reliability of CGCMs simulating the capacitor effect. Thus, the purpose of present study is to evaluate the biases of IOBM and its capacitor effect in CMIP3 and CMIP5 models. We want to address three questions: First, what lead to the IOBM bias, the atmospheric or oceanic processes, or both of them? Second, what cause the biases of these processes? Third, how do CMIP models simulate the capacitor effect? The rest of the paper is organized as follows. Section 2 describes the CMIP models, data and methods. An overall view of IOBM simulation in CMIP models is provided in Sect. 3. Section 4 evaluates the main processes in the evolution of IOBM and its influence to the NWP, including atmospheric processes, oceanic processes and the capacitor effect. Section 5 presents a synthesis of IOBM biases in each model. Section 6 provides the summary.

2 Data and methods

This study is based on the CMIP3 climate of 20th century (20C3M) and CMIP5 historical scenario simulations. The 20C3M experiments were conducted based on observed history of anthropogenic and natural forcing from 1900 to 1999, and from 1870 to 2006 for the historical experiments. The detailed information is referred to the following web site: http://cmip-pcmdi.llnl.gov/. In this study, 30 years simulations covering 1970–2000 from 15 CMIP3 and 32 CMIP5 models are used. Table 1 lists the names, institutions and countries of models. Monthly mean outputs are

Table 1 The CMIP models used in this study

NO.	Model name	Institute (country)
1	ACCESS1.0	Commonwealth Scientific and Industrial Research Organisation and Bureau of Meteorology (Australia)
2	BCC-CSM1.1	Beijing Climate Center (China)
3	BCC-CSM1.1-M	
4	CanCM4	Canadian Centre for Climate Modelling and Analysis (Canada)
5	CanESM2	
6	CCSM4	National Center for Atmospheric Research (USA)
7	CESM1-BGC	
8	CESM1-CAM5	
9	CESM1-FASTCHEM	
10	CESM1-WACCM	
11	CMCC-CM	Centre National de Recherches Météorologiques/Centre Européen de Recherche et Formation Avancée en Calcul Scientifique (France)
12	CNRM-CM5	Centre National de Recherches Meteorologiques (France)
13	CSIRO-Mk3.6.0	Commonwealth Scientific and Industrial Research Organisation in collaboration with the Queensland Climate Change Centre of Excellence (Australia)
14	FGOALS-g2	LASG, Institute of Atmospheric Physics, Chinese Academy of Sciences, and CESS, Tsinghua University (China)
15	GFDL-CM3	Geophysical Fluid Dynamics Laboratory (USA)
16	GFDL-ESM2G	
17	GFDL-ESM2 M	
18	GISS-E2-R	NASA Goddard Institute for Space Studies (USA)
19	HadGEM2-CC	Met Office Hadley Centre (UK)
20	HadGEM2-ES	
21	INM-CM4	Institute for Numerical Mathematics (Russia)
22	IPSL-CM5A-LR	Institut Pierre Simon Laplace (France)
23	IPSL-CM5A-MR	
24	IPSL-CM5B-LR	
25	MIROC5	Japan Agency for Marine-Earth Science and Technology, Atmosphere and Ocean Research Institute (The University of Tokyo), and National Institute for Environmental Studies (Japan)
26	MIROC-ESM	
27	MIROC-ESM-CHEM	
28	MPI-ESM-LR	Max Planck Institute for Meteorology (MPI-M) (Germany)
29	MPI-ESM-MR	
30	MRI-CGCM3	Meteorological Research Institute (Japan)
31	NorESM1-M	Norwegian Climate Centre (Norway)
32	NorESM1-ME	
33	bccr_bcm2_0	Bjerknes Centre for Climate Research (Norway)
34	cccma_cgcm3_1_t47	Canadian Centre for Climate Modelling and Analysis (Canada)
35	gfdl2_0	Geophysical Fluid Dynamics Laboratory (USA)
36	gfdl2_1	
37	giss_aom	NASA Goddard Institute for Space Studies (USA)
38	giss_model_e_h	
39	giss_model_e_r	
40	fgoals_g1_0	LASG, Institute of Atmospheric Physics, Chinese Academy of Sciences (China)
41	ipsl_cm4	Institute Pierre Simon Laplace (France)
42	miroc3_2_ hires	Center for Climate System Research (Japan)
43	miroc3_2_ medres	

Table 1 continued

NO.	Model name	Institute (country)
44	mpi_echam5	Max Planck Institute for Meteorology (Germany)
45	mri_cgcm2_3_2a	Meteorological Research Institute (Japan)
46	ncar_pcm1	National Center for Atmospheric Research (USA)
47	ukmo_hadgem1	Met Office Hadley Centre (UK)

No. 1–32 are CMIP5 models and No. 33–47 are CMIP3 models

used, including SST, sea surface height (SSH), precipitation, 850 and 200 hPa wind, latent heat flux (LHF), short wave radiation (SWR), 200 hPa geopotential height. Only one member ('r1i1p1') run of each model is analyzed. The observations include the following: (1) Hadley Centre Sea ICE and Sea Surface Temperature dataset (HadISST) with 1° × 1° horizontal resolution covers the period from January 1870 to the present (Rayner et al. 2003); (2) Monthly 850 and 200 hPa wind, LHF, SWR, 200 hPa geopotential height from the NCEP/NCAR reanalysis product with 2.5° × 2.5° horizontal resolution covers the period from January 1948 to the present (Kalnay et al. 1996); (3) Simple Ocean Data Assimilation (SODA) product of version 2.1.6 with 0.5° × 0.5° horizontal resolution covers the period from January 1958 through December 2008 (Carton et al. 2005; Carton and Giese 2008); (4) NOAA's Precipitation Reconstruction (PREC) with 2.5° × 2.5° horizontal resolution covers the period from January 1948 to the present (Chen et al. 2002). All CMIP outputs are interpolated to the resolution of observation and reanalysis data except for the SSH, which are interpolated to a 1° × 1° grid, the same as SST for calculation purpose.

The monthly mean climatology is first calculated for the study period. Then, interannual anomalies are computed as the departure from the climatology. This study focuses on the interannual variability. To extract interannual signals, we perform a 3-month running average to reduce intraseasonal variability and remove the least squares trend both in model outputs and observation. Hereafter, any month in the developing years of ENSO are identified by suffix (0), whereas any month in the decaying years of ENSO are identified by suffix (1). SON represents the seasonal mean in September–October–November, DJF represents the seasonal mean in December–January–February, and so on. The Niño3.4 index is defined as SST anomalies averaged over the central and eastern equatorial Pacific (5°S–5°N, 170°–120°W) in D(0)JF(1). Regression and correlation analysis are used. The multi-model ensemble (MME) is calculated by averaging over the models with equivalent weight. The processes of calculating MME are as follows: results are analyzed in each model respectively and then the MME is calculated. Therefore, the MME results eliminate the inter-model spread, reflecting the average performance of models.

3 IOBM in CMIP models

ENSO is a major forcing for IOBM (Klein et al. 1999; Alexander et al. 2002; Xie et al. 2002; Lau and Nath 2003; Du et al. 2009; Schott et al. 2009; Tao et al. 2014). The simulation of IOBM depends largely on the simulation of the ENSO in CMIP models (Saji et al. 2006; Du et al. 2013; Tao et al. 2015). In this section, seasonal mean SST, precipitation, circulation and SSH anomalies related to ENSO in 15 CMIP3 models and 32 CMIP5 models are respectively examined to evaluate the general characteristics of IOBM in the state-of-the-art CGCMs. Figure 1 shows the evolution of SST, 850 hPa wind and SSH anomalies with respect to D(0)JF(1) Niño3.4 index in observation, CMIP3 and CMIP5 MME. The evolution of precipitation, 200 hPa potential velocity and divergent wind component anomalies over the Indo-western pacific with respect to D(0)JF(1) Niño3.4 index in observation, CMIP3 and CMIP5 MME are shown in Fig. 2.

3.1 SST pattern

Over the equatorial Pacific, the ENSO-related SST anomaly patterns extend more westward in CMIP MME than in the observation during the mature phase (Fig. 1b, f, j), which has been mentioned in previous studies (Collins et al. 2010; Kim and Yu 2012; Gong et al. 2013; Bellenger et al. 2014; Gong et al. 2014; Ham and Kug 2014; Huang et al. 2014; Zhang and Sun 2014; Tao et al. 2015). The equatorial western Pacific (WP) SST anomalies persist into boreal summer in CMIP MME, but are almost dissipated in observation. Over the TIO, the SST anomaly pattern is characterized by the positive Indian Ocean Dipole Mode in fall (IODM; Saji et al. 1999; Webster et al. 1999), with warming in the west Indian Ocean and cooling in the east Indian Ocean (EIO; Fig. 1a). The EIO cooling dissipates and the whole basin warms up in subsequent winter (Fig. 1b), and persists into summer (Fig. 1c, d). Both CMIP3 and CMIP5 MME results generally capture the evolution of SST anomaly pattern from IODM to IOBM (Fig. 1e–h, i–l). However, there are some discrepancies between the observation and CMIP MME. The SIO SST anomalies are weaker in MME, and the cooling extends too westward during SON (Fig. 1e, i). Weaker SIO SST

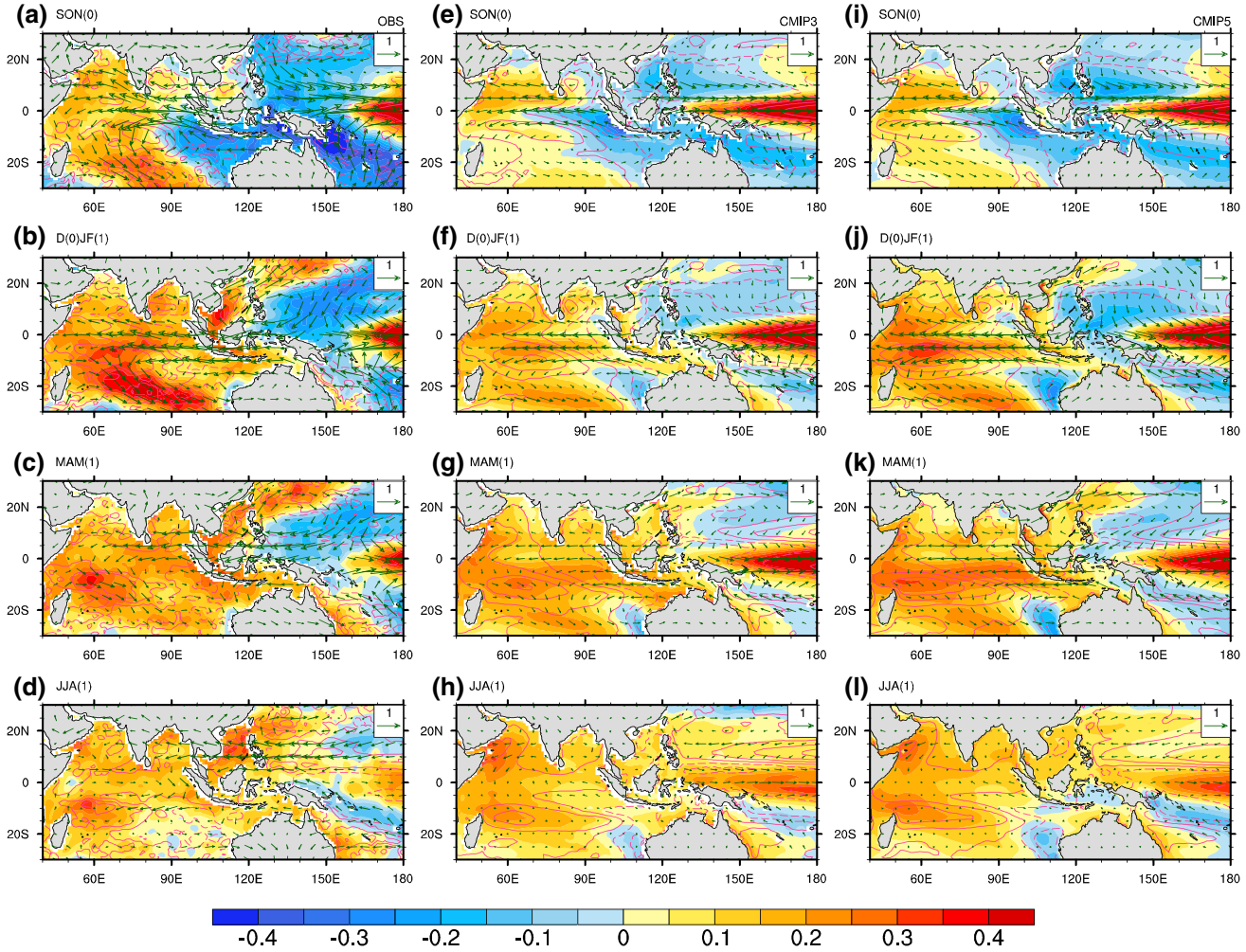

Fig. 1 Regression of SST (*shaded*, °C), 850 hPa wind (*vector*, ms^{-1}) and SSH (*contour*, observation: CI 2 cm, CMIP: CI 1 cm) with respect to D(0)JF(1) Niño3.4 index during SON(0), D(0)JF(1), MAM(1) and JJA(1) for observation (*left panels*, **a**–**d**), CMIP3 (*middle panels*, **e**–**h**) and CMIP5 (*right panels*, **i**–**l**) MME

anomalies still exist in D(0)JF(1) (Fig. 1f, j). Nevertheless, the IOBM patterns are comparable to observation in MAM(1) and JJA(1) (Fig. 1g, h, k, l). Note that the SST anomalies off the northwest coast of Australia in the simulations are always negative, which are due to a westward shift of equatorial Pacific SST anomalies and will be interpreted in the next section.

3.2 Indo-western Pacific precipitation

The most important feature of ENSO in terms of climate impacts and teleconnections is its impact on precipitation and large-scale circulation (e.g., Bellenger et al. 2014). In SON(0), suppressed rainfall associated with ENSO-induced upper level convergence is located over the Maritime Continent (MC) and equatorial EIO while enhanced rainfall is found over the equatorial WP (Fig. 2a). During D(0)JF(1) and MAM(1), especially the MAM season, the suppressed rainfall in the EIO decays rapidly and the center moves eastward to the Philippine Sea in accompany with the movement of upper level convergence (Fig. 2b, c). Note that there are also dry anomalies over the North Indian Ocean (NIO) in MAM(1), which is mainly forced by local air–sea interaction. It should be mentioned that the mechanism of suppressed rainfall associated with upper level convergence over the NWP in JJA(1) is different from the previous three seasons (Fig. 2d). With the disappearance of tropical Pacific SST anomalies, the Indian Ocean SST anomalies gradually play an important role (Yang et al. 2007, 2009, 2010; Xie et al. 2009; Chowdary et al. 2011).

In general, the CMIP MME captures the eastward movement of observed precipitation anomalies associated with the ENSO turnabout. However, the rainfall anomalies over the whole Indo-western pacific region are weaker

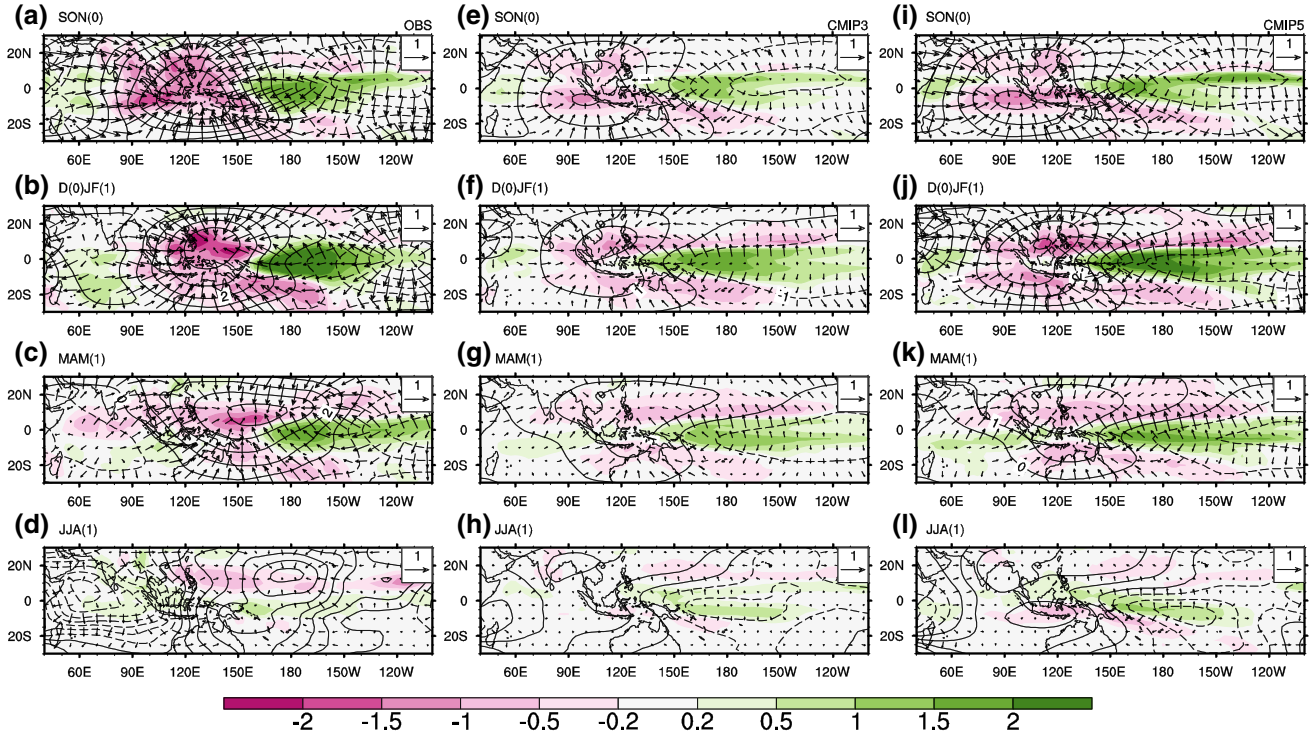

Fig. 2 As in Fig. 1, but for precipitation (*shaded*, mm), 200 hPa potential velocity (*contour*, first three *rows*: CI 1×10^6 m^2 s^{-1}, *last row* CI 2.5 $\times$ 10^5 m^2 s^{-1}) and divergent wind component (*vector*, m s^{-1}). *Solid* and *dashed lines* represent positive and negative values, respectively. **a**, **e**, **i**, SON(0). **b**, **f**, **j**, D(0)JF(1). **c**, **g**, **k** MAM(1). **d**, **h**, **l** JJA(1)

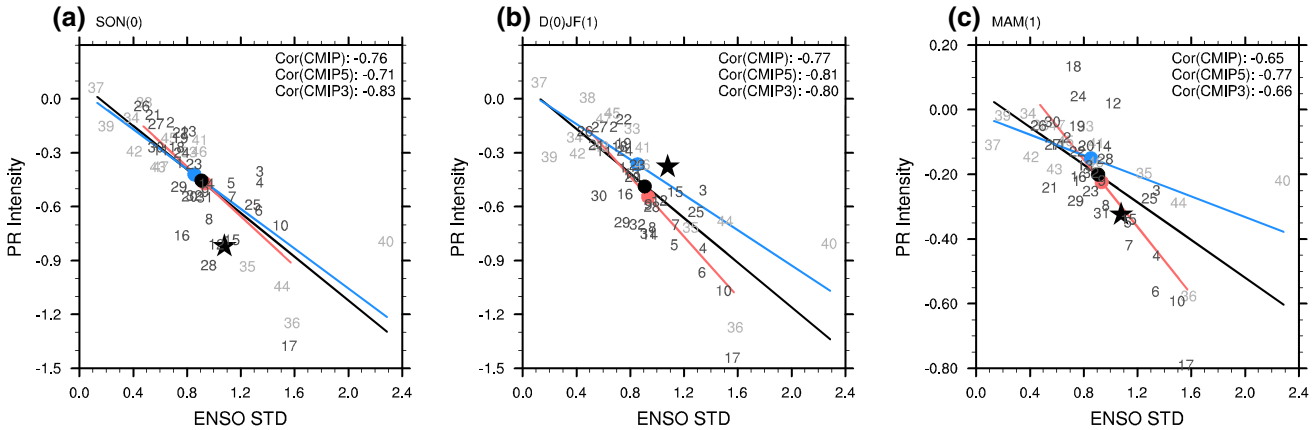

Fig. 3 Scatter diagram of D(0)JF(1) ENSO standard deviations (abscissa) versus **a** SON(0) suppressed rainfall intensity (ordinate) ranged from the EIO to MC (20°S–20°N, 90°–120°W); **b** D(0)JF(1) suppressed rainfall intensity (ordinate) ranged from the EIO to MC (20°S–20°N, 90°–120°W); **c** MAM(1) suppressed rainfall intensity (ordinate) in the NIO (0°–20°N, 60°–100°W). Numbers represent the model numbers listed in Table 1, and the *star* represents the observation. The *blue*, *red* and *black solid circles* are the MME of CMIP3, CMIP5 and all CMIP models respectively. The *blue*, *red* and *black lines* are the best fit lines for the scatters of CMIP3, CMIP5 and all CMIP models, respectively. The correlation coefficients of CMIP3, CMIP5 and all CMIP models are on the *top corner* of each figure. These comments are all the same in following figures

than observation (Fig. 2e–l). Besides, both wet and dry anomalies extend westward (Fig. 2e–g, i–k), corresponding to the westward shift of SST anomalies in simulations (Fig. 1e–g, i–k). Figure 3 presents the relationship of ENSO and suppressed rainfall in CMIP models. The rainfall intensity is largely controlled by ENSO intensity in models. In SON(0) and MAM(1), slightly weaker ENSO intensity leads to weaker MME rainfall intensity in

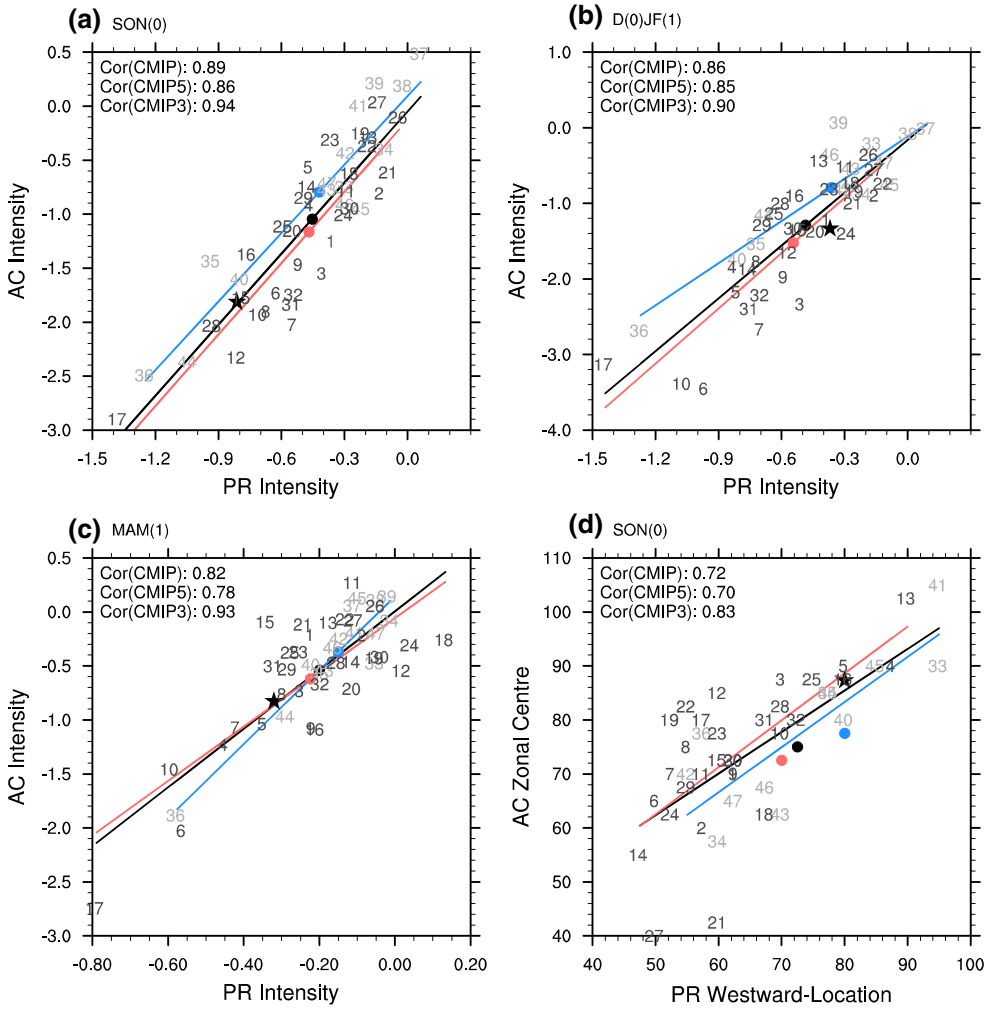

Fig. 4 Scatter diagram of the suppressed rainfall and SIO anticyclone: **a**, **b**, **c** the suppressed rainfall intensity (abscissa) versus the anticyclone intensity (ordinate) in SON(0), D(0)JF(1), MAM(1), respectively; **d** the west boundary of suppressed rainfall over the SIO (abscissa) versus the longitude of maximum zonal wind anomalies in the north flank of the anticyclone (ordinate) in SON(0)

the models (Fig. 3a, c), which is consistent with Bellenger et al. (2014). However, the rainfall intensity in the models is comparable to or stronger than in the observation during D(0)JF(1) (Fig. 3b) due to the west bias of dry anomalies. The JJA(1) rainfall anomalies over the NWP are weaker in MME corresponding with weaker anomalous anticyclone, which is more likely forced by the WP SST anomalies (Figs. 1h, l, 2h, l).

3.3 The SIO anticyclone

During the fall of the ENSO developing year, SON(0), there are anticyclonic wind anomalies dominating the SIO (Fig. 1a). This anticyclone is a Rossby wave response to the suppressed rainfall (Fig. 2a; Matsuno 1966; Gill 1980; Wang et al. 2003). Resulting from the effect of mean monsoon circulation on the Rossby wave response (Wang and Xie 1996; Xie and Wang 1996; Wang et al. 2003), the anticyclone moves southward in D(0)JF(1). In the decay phase of ENSO, MAM(1), the anticyclone weakens and moves northwestward owing to the strengthened meridional SST gradient after the SWIO warming, shaping the antisymmetric wind pattern (Fig. 1c; Xie et al. 2002; Wu et al. 2008; Du et al. 2009). Moreover, there are climatology easterly trade winds over the equator in early spring. To the south flank of antisymmetric wind pattern over the SIO are northwesterly wind anomalies, which weaken the southeasterly trade winds and sustain the warming there. The northeasterly wind anomalies in the north flank strengthen the climatology northeasterly winds and reduce the NIO warming. Thus, the antisymmetric wind pattern also maintains the meridional SST gradient in return (Du et al. 2009). The anomalous anticyclonic circulation almost dissipates in JJA(1). Once again, the MME results capture the evolution of anomalous anticyclone (Fig. 1e–l). However, the overall intensity of the anticyclone is weaker,

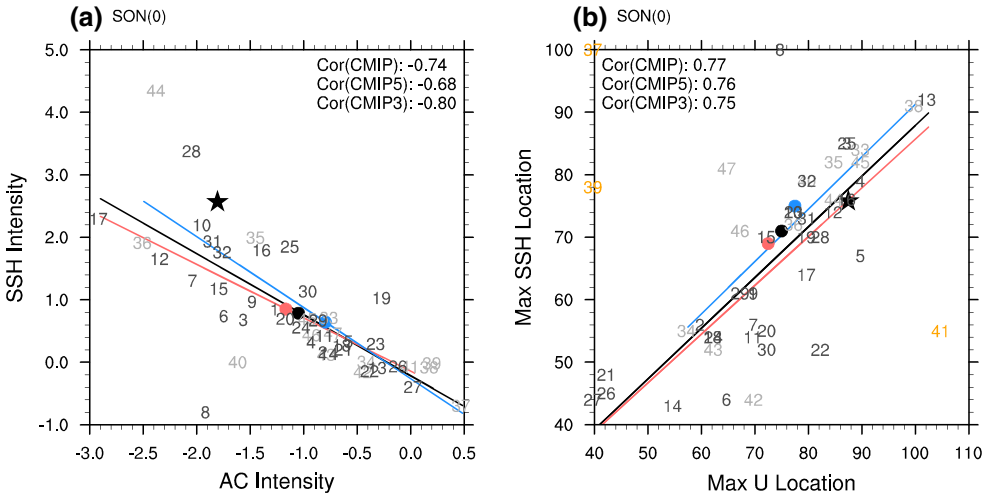

Fig. 5 Scatter diagram of the SIO anticyclone and SSH in SON(0): **a** the anticyclone intensity (abscissa) versus SSH intensity (ordinate); **b** the longitude of maximum zonal wind anomalies in the north flank of the anticyclone (abscissa) versus the longitude of maximum SSH change (ordinate). The *yellow numbers* represent the models not contained in calculating the best fit lines and correlation coefficients

especially to the south flank of it. The anticyclone intensity is highly correlated to the suppressed rainfall intensity in models (Fig. 4). The simulated anticyclone is comparable to observation in D(0)JF(1) due to stronger precipitation anomalies, while it is weaker in SON(0) and MAM(1). As discussed in Sect. 3.2, dry anomalies and anomalous circulation in MAM(1) are response to local SST anomalies, which emphasizes the importance of atmosphere–ocean coupling in this season (Wu et al. 2008). West bias also exists in the anticyclonic wind anomalies (Fig. 1e–g, i–k), which is related to the west bias of precipitation anomalies (Figs. 2e–g, i–k, 4d).

3.4 The response of thermocline

In SON(0), the downwelling Rossby wave is forced by the anticyclonic circulation in the SIO and propagates westward, deepening the thermocline in SWIO and raising the SST there in D(0)JF(1) and MAM(1) (Fig. 1a–c; Xie et al. 2002; Du et al. 2009; Wu and Yeh 2010). However, the thermocline change is weaker in MME, especially during SON and MAM, which is related to weaker anticyclone (Fig. 1e–l). Figure 5 shows the relationship between the anticyclone and SSH in SON(0). Weaker thermocline anomalies correspond to weaker anticyclone in CMIP models, indicating a positive correlation between them (Fig. 5a). Besides, owing to the west bias of anticyclone simulation, the maximum thermocline anomalies extend too far west in models (Fig. 5b), and there is no significant westward oceanic process in MME (Fig. 1e–l). Some models show deepened thermocline without the propagation of Rossby wave, such as CCSM4, GFDL-CM3, GFDL-ESM2M and so on (figures not shown). In these models, the Ekman response may play an important role in the thermocline change, which is associated with the west bias of anticyclone. Therefore, both the oceanic Rossby wave and local wind curls can adjust the tropical SWIO thermocline in CMIP models, as first mentioned by Du et al. (2013).

4 Main processes of IOBM and its influence to the NWP

There exist complex physical processes in the evolution of IOBM. From the thermodynamic aspect, ENSO causes changes in the atmosphere via the atmospheric bridge (Lau and Nath 1996; Klein et al. 1999) or TT (Chiang and Sobel 2002; Chiang and Lintner 2005) mechanism, and the atmospheric changes in turn affect SST through the NHF. From the oceanic dynamic aspect, ENSO-induced oceanic processes play a significant role in IOBM warming (Murtugudde and Busalacchi 1999; Yu and Rienecker 1999), especially the tropical SWIO (Xie et al. 2002). Moreover, local air-sea interactions can modulate the SST distribution of IOBM in different seasons (Wu et al. 2008; Du et al. 2009).

The IOBM warming persists into summer when the equatorial Pacific SST anomalies have dissipated, characterized by a Matsuno-Gill (Matsuno 1966; Gill 1980) pattern with warm tropospheric Kelvin wave eastward in atmosphere (Yang et al. 2007; Xie et al. 2009; Yang et al. 2010). The equatorial low pressure in the Kelvin wave drives northeasterly winds, inducing low level divergence and suppressing convection over the NWP. In turn, the suppressed convection further amplifies the divergence, forming a positive feedback (Xie et al. 2009). This process is called as the TIO capacitor effect (Yang et al. 2007; Xie

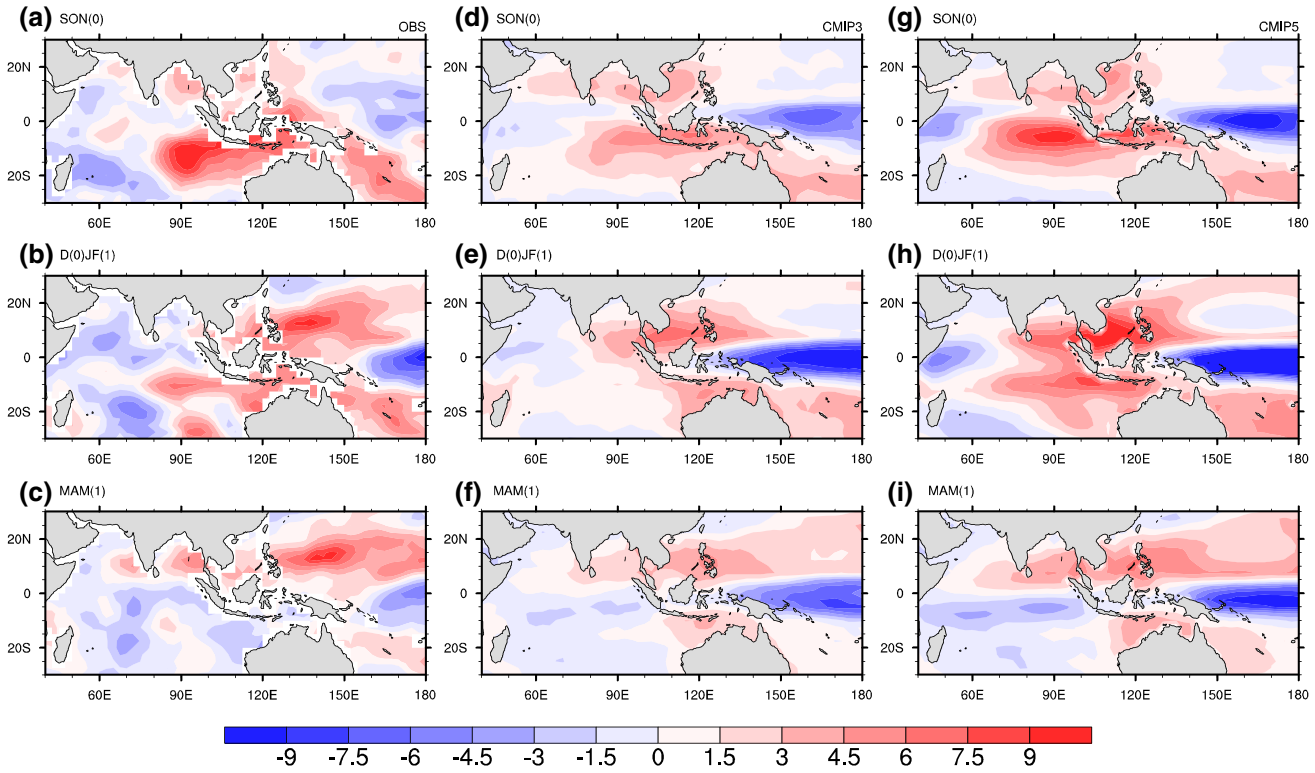

Fig. 6 Regression of SWR (Wm^{-2}, downward positive) with respect to D(0)JF(1) Niño3.4 index during SON(0), D(0)JF(1) and MAM(1) for observation (*left panels*, **a**–**c**), CMIP3 (*middle panels*, **d**–**f**) and CMIP5 (*right panels*, **g**–**i**) MME

et al. 2009; Yang et al. 2010). In this section, the biases of these physical processes are investigated to understand how the CMIP models simulate IOBM and its influence.

4.1 Atmospheric processes

NHF is the essence of atmospheric bridge or TT mechanism. In general, NHF could be divided into four components: long wave radiation, SWR, LHF and sensible heat flux. The SWR and LHF account for most of NHF in tropical oceans. Analysis of Du et al. (2009) suggests that the change in wind speed dominates the atmospheric forcing component of LHF over the whole basin. In particular, the wind-evaporation-SST (WES) feedback (Xie and Philander 1994) is the major mechanism in wind-induced LHF change. Different from the LHF, SWR effect is important in the EIO, especially the southeast Indian Ocean (SEIO; Klein et al. 1999; Wu et al. 2008; Du et al. 2009; Wu and Yeh 2010). The cloud-radiation-SST (CRS) feedback (Ramanathan and Collins 1991) plays a major role in SWR change.

Figures 6 and 7 illustrate the evolution of ENSO-induced SWR and LHF anomalies in observation and CMIP MME. On one hand, the SWR pattern is similar to the rainfall pattern in observation and CMIP MME, indicating the effect of CRS feedback (Figs. 2 and 6), which is in agreement with previous studies (Klein et al. 1999; Wu et al. 2008; Du et al. 2009; Wu and Yeh 2010). In addition, the SWR anomalies in the MME are comparable to or stronger than the observation along with a west bias, especially in DJF (Fig. 6). On the other hand, due to the effect of WES feedback, the downward LHF anomalies are located to north and south flank of the SIO anticyclone (Figs. 1, 7), which is also mentioned before (Klein et al. 1999; Wang et al. 2003; Wu et al. 2008; Wu and Yeh 2010). The simulated LHF anomalies are weak and shift westward due to weak and west bias of anomalous anticyclone (Fig. 1e–l).

To further confirm the relationship between SWR and precipitation, the corresponding scatter diagrams are presented in Figs. 8a–c. More suppressed rainfall grid-numbers correspond to more downward SWR grid-numbers in observation. Compared to the observation, the ratio of SWR grid-numbers versus rainfall grid-numbers is usually larger in the models, indicating that the CRS feedback is stronger in most models (Fig. 8a–c). Figure 9a clearly shows the CRS feedback in CMIP MME and individual models compared with the observation. A stronger CRS feedback exists in the CMIP5 models and their MME than observation, and slight weaker CRS feedback in CMIP3 MME. For individual models, 32 out of 47, about 70 % of

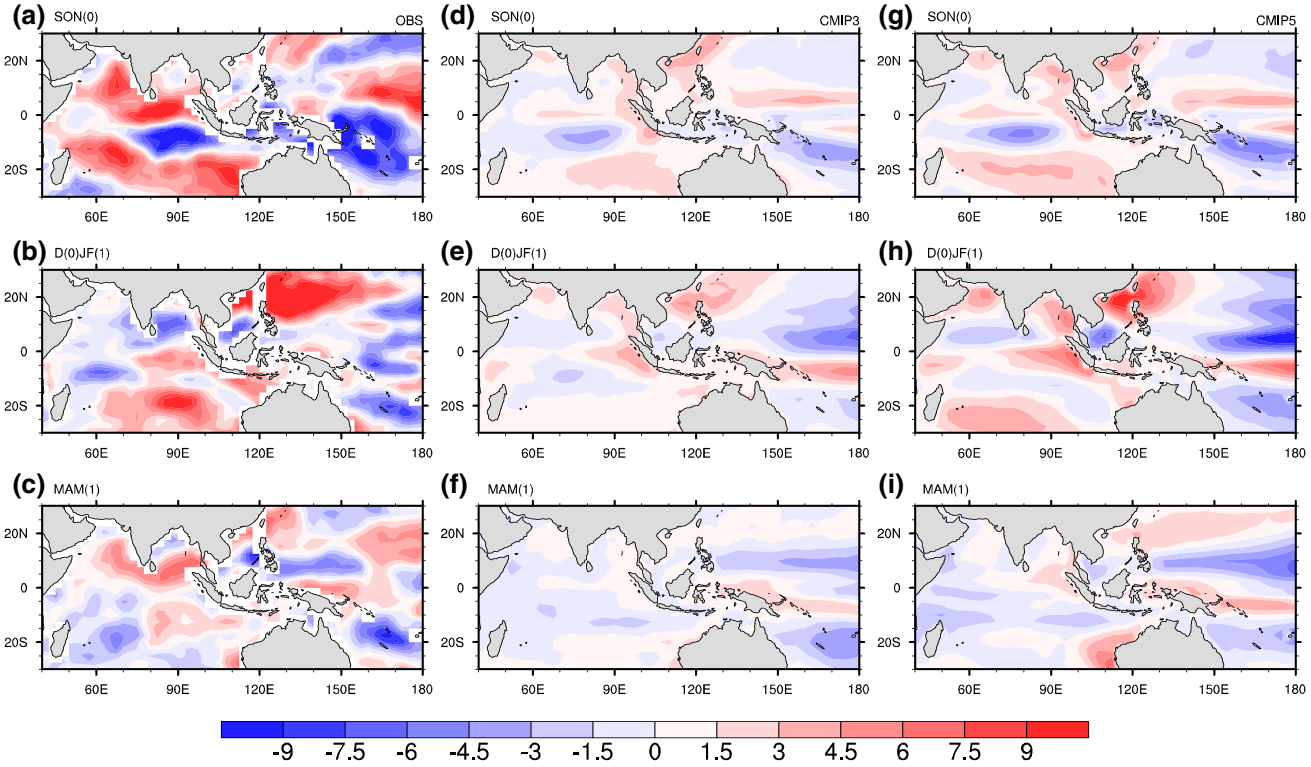

Fig. 7 As in Fig. 6, but for the LHF (Wm^{-2}, downward positive)

the CMIP models show a stronger feedback. Thus, there is a strong bias of CRS feedback in state-of-the-art CGCMs.

The SIO anticyclone intensity is highly correlated with the downward LHF grid-numbers in CMIP models, and the overall weak bias of SIO anticyclone induces overall less downward LHF grid-numbers (Fig. 8d–f). Moreover, the stronger intensity of SIO anticyclone tends to correspond to relatively less LHF grid-numbers in most models, suggesting a weaker WES feedback (Fig. 8d–f). The WES feedback is weaker in CMIP MME, and also in 38 out of 47 (about 80 %) CMIP models (Fig. 9b). Thus, the WES feedback is weaker in models.

The CMIP models simulate stronger SWR anomalies and more downward SWR grid-numbers due to the west bias of rainfall anomalies and strong bias of CRS feedback (Figs. 2e–l, 6, 8a–c, 9a). The models simulate weaker LHF anomalies and less downward LHF grid-numbers than observation due to the weak bias of SIO anticyclone and weak bias of WES feedback (Figs. 1e–l, 7, 8d–f, 9b). Figure 8g–i show the scatter diagram of the downward SWR grid-numbers versus downward LHF grid-numbers. There are more LHF grid-numbers than SWR grid-numbers in observation, while in CMIP models, there tends to be more SWR grid-numbers than LHF grid-numbers.

Though the models simulate stronger SWR and weaker LHF anomalies, the sum of them are slightly weaker than observation except for the DJF season, indicating compensation of errors in IOBM simulation (Fig. 10). The NHF pattern is similar to the LHF pattern in observation (Figs. 7a–c, 10a–c). However, due to stronger SWR and weaker LHF anomalies, the NHF pattern is similar to the SWR pattern in CMIP MME (Figs. 6d–i, 10d–i). Thus, there are differences between the observation and MME in detail. In SON(0), upward NHF anomalies in the equatorial Indian Ocean are weaker in CMIP3 MME (Fig. 10d), and even disappear in CMIP5 MME (Fig. 10g). Observation shows downward NHF anomalies over the SEIO in D(0)JF(1), but there are downward NHF anomalies over the EIO, especially the northeast Indian Ocean in CMIP MME (Fig. 10b, e, h). The NHF anomalies are slightly weaker in MAM(1). All these discrepancies in CMIP models can be attributed to the strong bias of SWR anomalies and weak bias of LHF anomalies. The cooling over the northwest coast of Australia in CMIP MME can partly be attributed to the weak downward NHF during DJF (Fig. 10b, c). Note that the NHF cannot explain the SST tendency over the whole basin, as tropical SWIO, both in observation and MME results (Fig. 10a, b, d, e, g, h), which have been pointed out in the introduction (Klein et al. 1999). Therefore, the next subsection will discuss how well the state-of-the-art CGCMs simulate the oceanic processes.

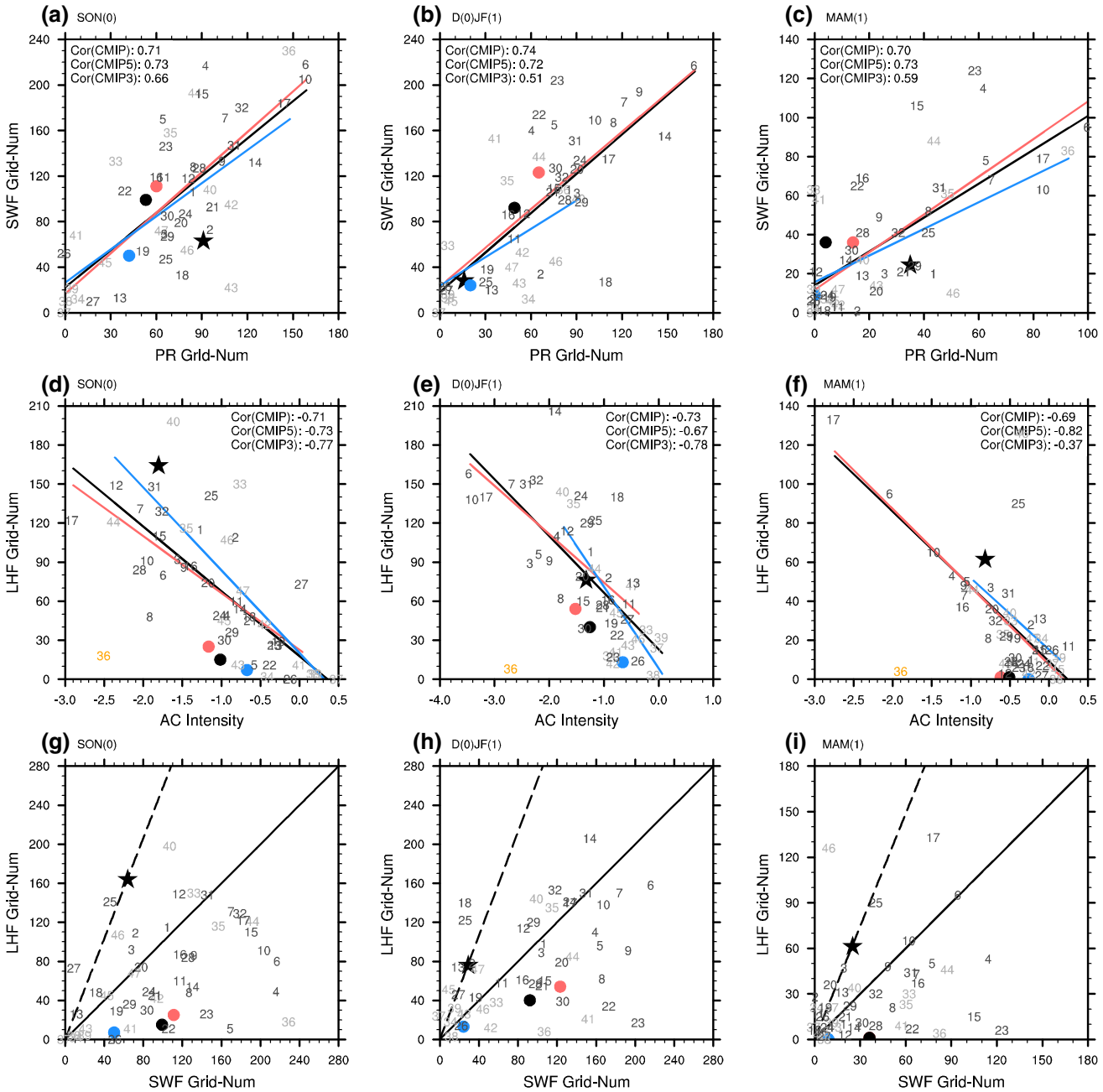

Fig. 8 Scatter diagram of the suppressed rainfall grid-numbers (abscissa; values ≤ -0.5) versus downward SWR grid-numbers (ordinate; values ≥ 3) over the TIO (20°S–20°N, 40°–100°W) in **a** SON(0), **b** D(0)JF(1), **c** MAM(1), respectively. **d**, **e**, **f** are as (**a**), (**b**), (**c**), but for the SIO anticyclone intensity (abscissa) versus downward LHF grid-numbers (ordinate; values ≥ 3). **g**, **h**, **i** are as (**a**), (**b**), (**c**), but for the downward SWR grid-numbers (abscissa; values ≥ 3) versus LHF grid-numbers (ordinate; values ≥ 3). The *yellow numbers* represent the models not contained in calculating the best fit lines and correlation coefficients. The *dashed lines* represent the ratio of downward LHF grid-numbers and SWR grid-numbers in observation

4.2 Oceanic processes

As discussed in Sect. 3.4, weak bias of SSH anomalies are due to weak bias of SIO anticyclone. However, the thermocline feedback is related to thermocline depth. The change of thermocline depth alone may not be sufficient for the thermocline feedback to operate in observation. For instance, if the climatology thermocline is deep, the feedback will be weak. How do the CMIP models simulate the climatology thermocline depth and the thermocline feedback over the SWIO?

Figure 11 shows seasonal mean SSH in observation, CMIP3 and CMIP5 MME. In observation, the climatology

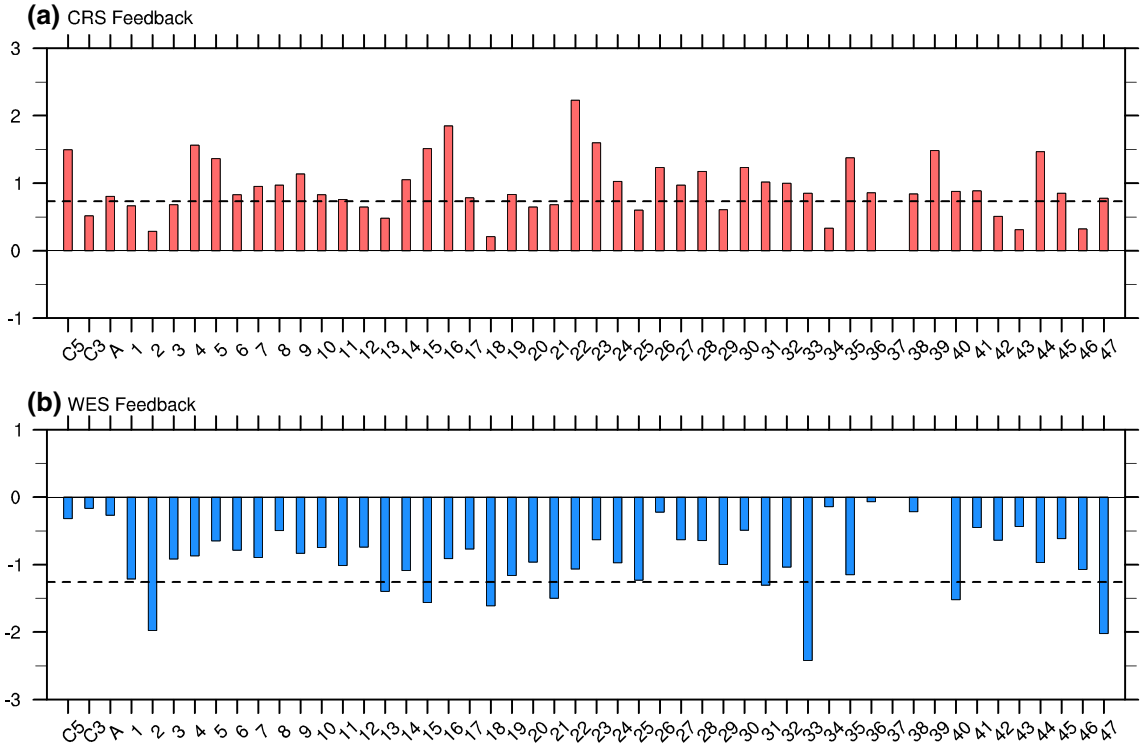

Fig. 9 The **a** CRS and **b** WES feedback index in CMIP5 ('C5'), CMIP3 ('C3'), all ('A') models MME and each model (*number*). The *dashed lines* represent the feedback index of observation. The CRS feedback index is the ratio between the downward SWR grid-numbers and suppressed rainfall grid-numbers in Fig. 8a–c. The WES feedback index is the ratio between the downward LHF grid-numbers and SIO anticyclone intensity in Fig. 8d–f. If a ratio's symbol is different from others or its value is much more abnormal than others, this outlier is set to zero in the figure

thermocline is shallow over the SWIO (Fig. 11a–d). The CMIP3 and CMIP5 MME show a similar pattern, but with the values overall larger than the observation. Over the SWIO, the CMIP3 simulated SSH is about 10 cm deeper than observation, and CMIP5 result is even 10 cm deeper than CMIP3. This indicates a deep bias of climatology thermocline in CMIP models. This bias is a consequence of overly stronger climatological easterly winds over the equatorial EIO (Cai and Cowan 2013; Li et al. 2015b, a).

There are significant SST anomalies induced by SSH change over the tropical SWIO in observation (Fig. 12a–d). The SWIO SST anomalies in MME are comparable to the observation (Fig. 13), which is first presented by Fig. 10 in Du et al. (2013), but with a larger area (Fig. 12e–l). Note that significant SSH-induced SST anomalies over the northwest coast of Australia cause cooling there from D(0)JF(1) to JJA(1) in CMIP MME. The NHF anomalies can only partly explain the cooling in D(0)JF(1), indicating a more important role of thermocline feedback (Fig. 12f–h, j–l). The stronger feedback there is possibly due to anomalous upwelling caused by the off-coast southeasterly winds, which is ultimately attributed to the west bias of anticyclone simulation (Fig. 1). Okumura and Deser (2010) revealed similar warm SST anomalies over the northwest coast of Australia owing to northwesterly winds in the dissipating phase of La Niña. Because of significant SSH-induced SST anomalies in observation during D(0)JF(1) and MAM(1), we pay more attention to these two seasons. Figure 13 also reveals a positive relationship between the ENSO-related SSH change and SSH-induced SST anomalies. The effect of climatology SSH has been removed from ENSO-related SSH anomalies in Fig. 13. In the CMIP models, the ratio of SSH-induced SST anomalies versus thermocline change is larger compared to the observation (Fig. 13), indicating a stronger thermocline feedback in models than in the observation. This conclusion is further demonstrated by Fig. 14. Thus, though the SSH anomalies are weaker in CMIP models, the SSH-induced SST anomalies are comparable to observation due to the strong bias of thermocline feedback.

4.3 The capacitor effect

The Indian Ocean capacitor effect is an important mechanism in TIO's influence on the NWP climate (Yang et al. 2007; Xie et al. 2009; Huang et al. 2010; Xie et al. 2010; Yang et al. 2010; Chowdary et al. 2011). The TIO warming can persist into JJA(1) in CMIP MME (Fig. 1h, l). How

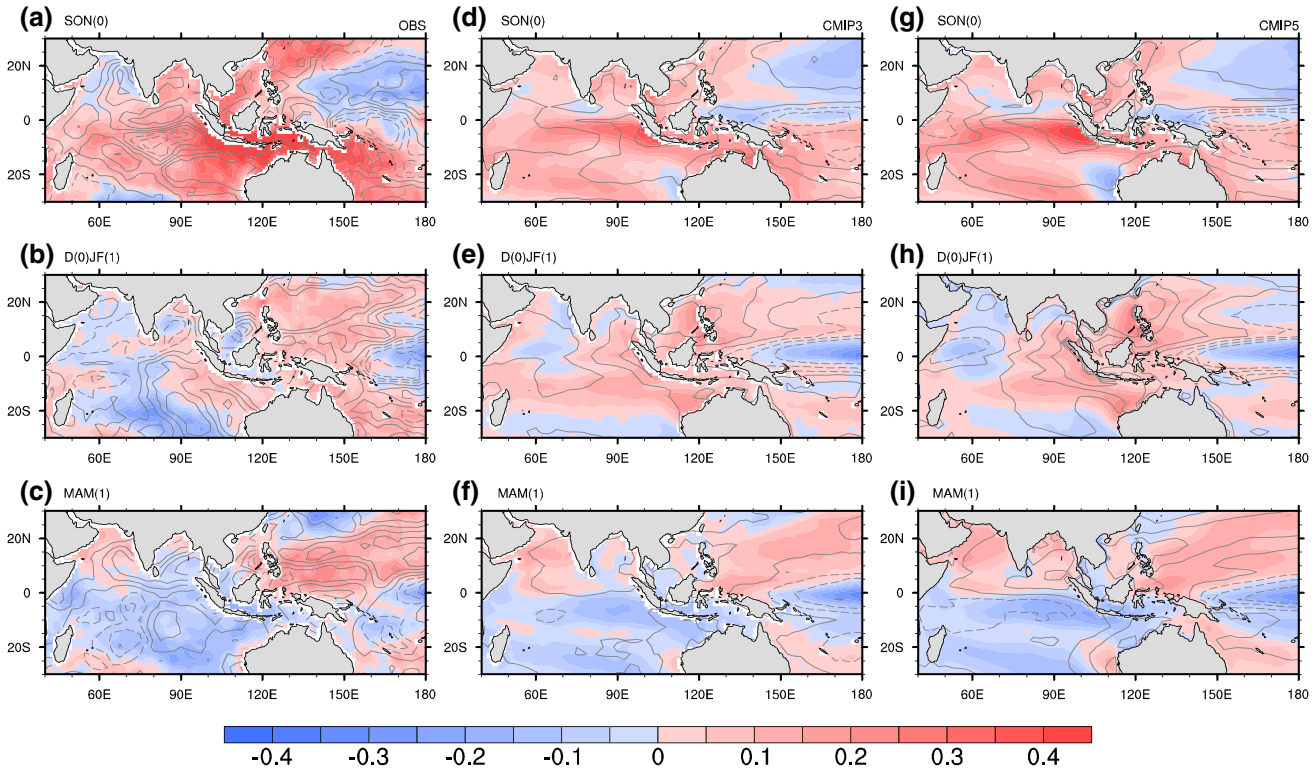

Fig. 10 As in Fig. 6, but for the SST tendency (shaded, °C) and NHF (contour, Wm^{-2}, downward positive)

do these models simulate the capacitor effect? Figure 15 shows regression of seasonal mean 200 hPa geopotential height and wind with respect to D(0)JF(1) Niño3.4 index in observation, CMIP3 and CMIP5 MME. In observation, the geopotential height displays a Matsuno-Gill (Matsuno 1966; Gill 1980) pattern with Kelvin wave eastward to the equatorial WP. Westerly winds dominate the Indo-western pacific region as a Kelvin wave response (Fig. 15a). As a result, anomalous anticyclone is induced at the north flank of the Kelvin wave (Fig. 1d). However, the Matsuno-Gill (Matsuno 1966; Gill 1980) pattern is weaker and displays a west bias in MME results, corresponding to the weaker and overly westward westerly winds (Fig. 15b, c). It seems that the westward Rossby wave from the Pacific triggers anomalous westerly winds, weakening easterly winds induced by the eastward Kelvin wave from the Indian Ocean in CMIP MME.

The tropical SST anomalies are the most effective way to warm the atmosphere above. The capacitor effect is mainly forced by the TIO warming in summer when ENSO has dissipated (Xie et al. 2009). However, the SST anomalies over the equatorial WP persist into JJA(1) in CMIP MME. Figure 16a further demonstrate this unrealistic SST anomalies. The equatorial WP SST anomalies persist longer than the observation in both CMIP3 and CMIP5 MME, which is possibly related to the overly westward extension of the ENSO warm tongue in state-of-the-art CGCMs (Collins et al. 2010; Kim and Yu 2012; Gong et al. 2013; Bellenger et al. 2014; Gong et al. 2014; Ham and Kug 2014; Huang et al. 2014; Zhang and Sun 2014; Tao et al. 2015). There are stronger westerly anomalies over the equatorial WP in most CMIP models, which indicates a Gill response to unrealistic WP SST anomalies (Fig. 16b). The unrealistic WP SST anomalies help the westward extension of Rossby wave and suppress the effect of eastward Kelvin wave, influencing the NWP anticyclone. Thus, on one hand, the westerly winds induced by the Rossby wave weaken the easterly winds induced by the Kelvin wave over the NWP. On the other hand, the WP warming forces the NWP anticyclone move farther north (about 5°) than observation (Fig. 1h, l). This suggests a major forcing from the Pacific (Fig. 2h, l), which is similar to the Pacific-Japan/East Asia–Pacific (PJ/EAP) teleconnection (Nitta 1987; Huang and Sun 1992).

5 Biases in each model

This section provides a synthesis of the IOBM biases in CMIP models. Considering different physical processes in the evolution of IOBM, four seasons are chosen for further study respectively. In SON(0), "pr_index_SON" indicates the SON(0) rainfall intensity as in Figs. 3 and

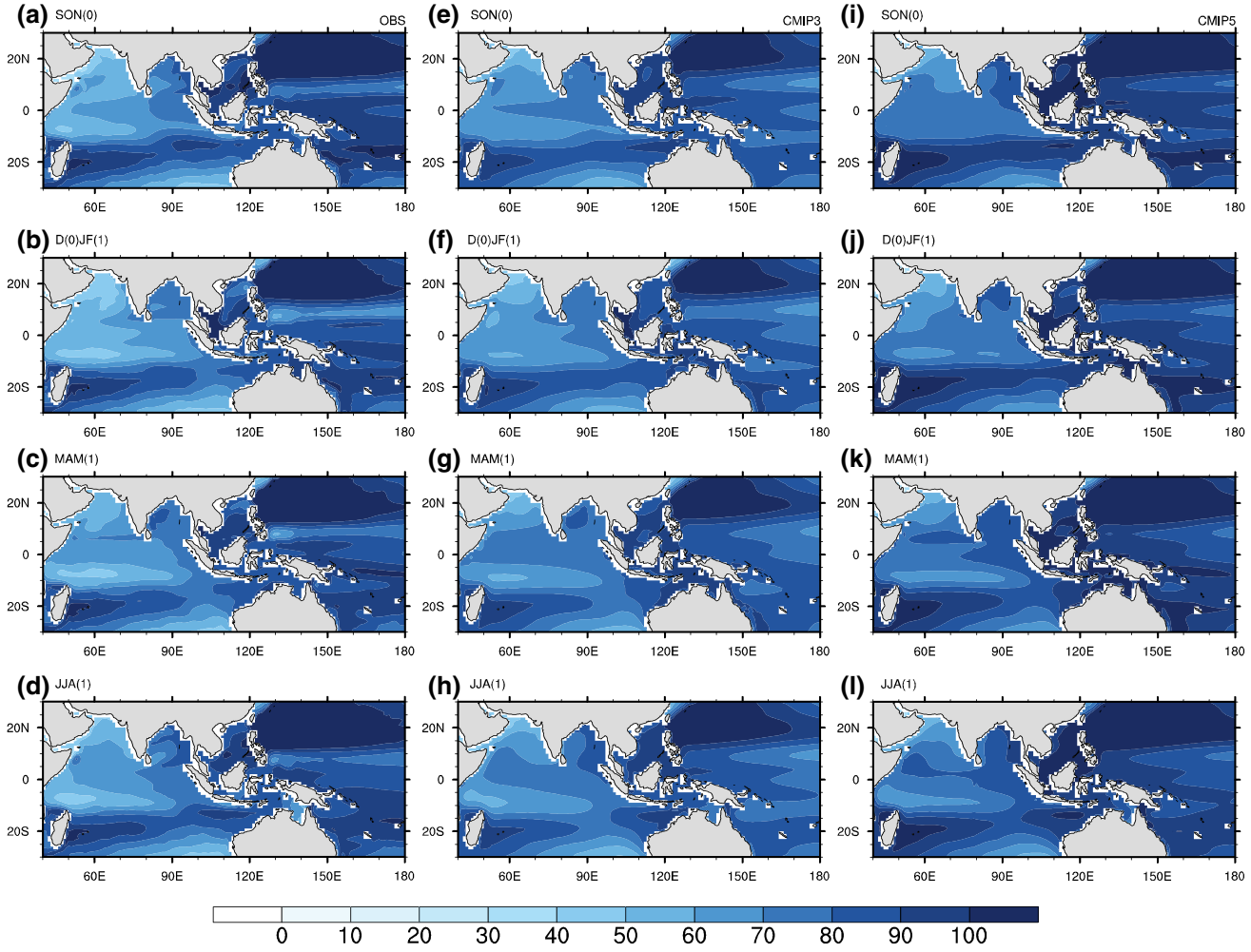

Fig. 11 The climatology SSH during SON(0), D(0)JF(1), MAM(1) and JJA(1) for observation (*left panels*, **a**–**d**), CMIP3 (*middle panels*, **e**–**h**) and CMIP5 (*right panels*, **i**–**l**) MME

4, "pr_num_SON" indicates the SON(0) suppressed rainfall grid-numbers over the TIO (20°S–20°N, 40°–100°W), "ac_index_SON" indicates the SON(0) SIO intensity as in Fig. 4, and the wind anomalies at north and south flank of SIO are represented as "Nu_index_SON" and "Su_index_SON", "sw_num_SON", "lh_num_SON", "nh_num_SON" indicate the downward SWR, LHF, NHF grid-numbers over the TIO, respectively, "u_max_lon_SON" and "ssh_max_lon_SON" are the longitude of maximum zonal wind anomalies and SSH change as in Fig. 5. In D(0)JF(1) and MAM(1), the first 8 variables are similar to those in SON(0), but for the corresponding seasons. The rest 4 variables are "clmssh_index", "ssh_index", "reg_ssh_sst", "IOBM", representing the tropical SWIO (15°–5°S, 50°–80°E) climatology SSH, ENSO-induced SSH anomalies, SSH-induced SST anomalies, IOBM intensity, respectively. In JJA(1), "IOBM_JJA" indicates the JJA(1) IOBM intensity, "nwpac_index_JJA" indicates the JJA(1) NWP anticyclone intensity, calculated as north flank (25°–35°N, 120°–160°E) minus south flank (5°–15°N, 120°–160°E), "wpsst_JJA" indicate the SST anomalies over the equatorial WP (5°S–5°N, 150°E–150°W). For each variable v and each model i, b_i is the bias normalized by CMIP3 + CMIP5 inter-model standard deviation (STD; $\sigma_{CMIP3+CMIP5}$) for each model, written as

$$b_i = \frac{v_i - v_{ref}}{\sigma_{CMIP3+CMIP5}}$$

For the relationship between the suppressed rainfall and SIO anticyclone as in Fig. 4, the intensity of suppressed rainfall anomalies in CMIP models are weaker in SON(0), reasonable in D(0)JF(1), and slightly weaker in MAM(1), corresponding with the bias change of SIO anticyclone, especially the south flank of anticyclonic wind anomalies ("pr_index", "ac_index", "Nu_index", "Su_index", in Fig. 17a–c). Note that the weak bias in

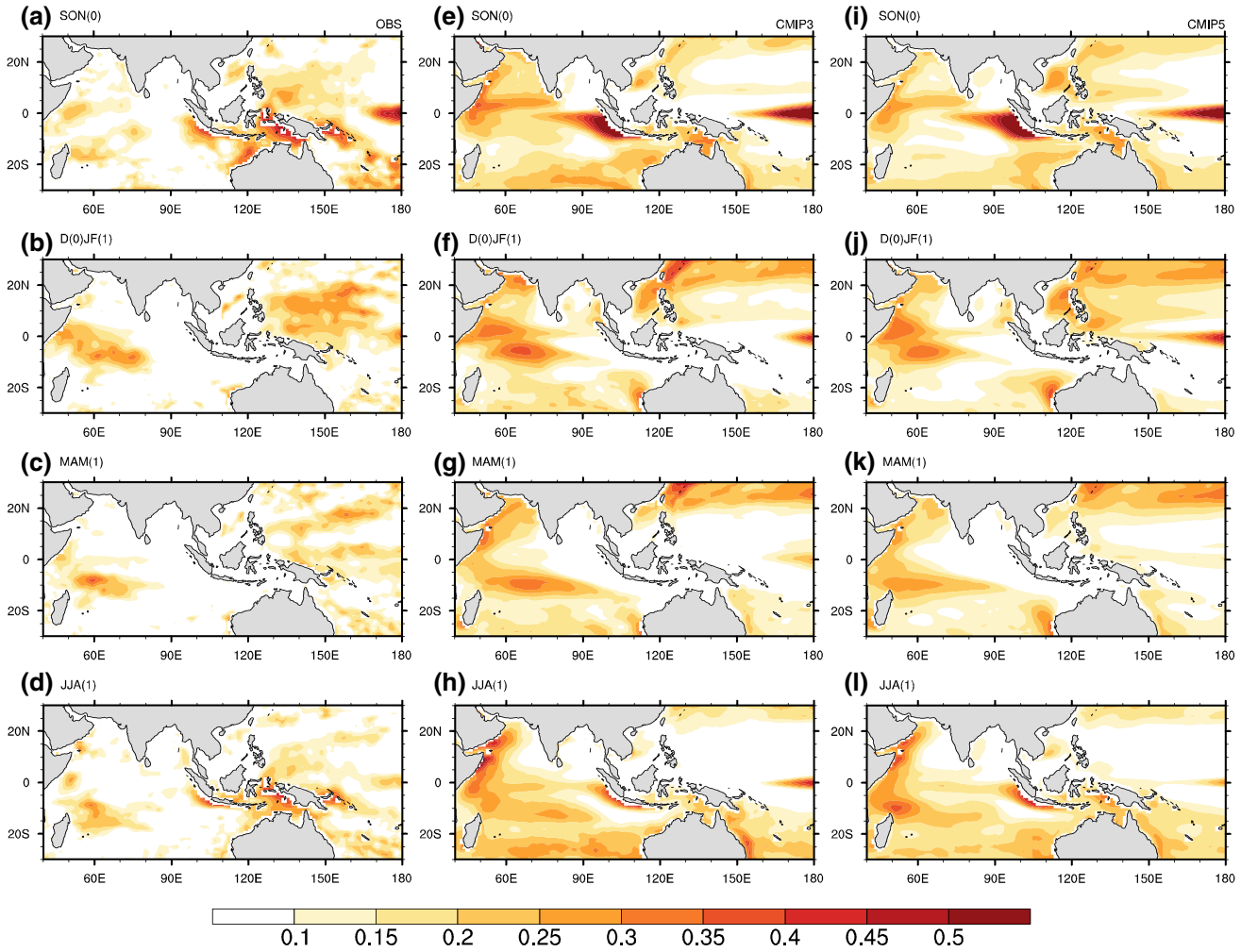

Fig. 12 Regression of SST anomalies with respect to SSH anomalies during SON(0), D(0)JF(1), MAM(1) and JJA(1) for observation (*left panels*, **a**–**d**), CMIP3 (*middle panels*, **e**–**h**) and CMIP5 (*right panels*, **i**–**l**) MME

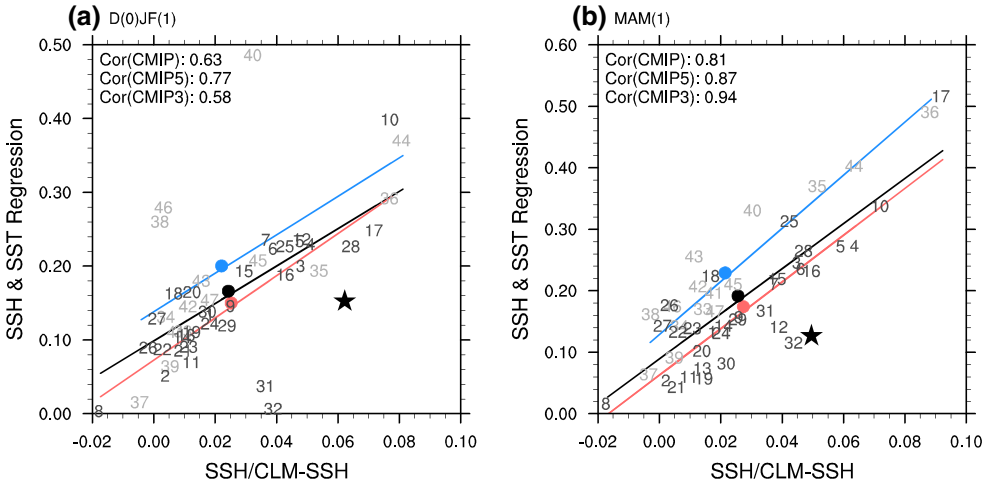

Fig. 13 Scatter diagram of the SSH change versus SSH-induced SST anomalies over the SWIO (15°S–5°S, 50°–80°E) in **a** D(0)JF(1), **b** MAM(1). The SSH change is calculated as the ratio of ENSO-induced SSH anomalies and climatology SSH depth in each season

MAM(1) anticyclone is more likely due to the weaker meridional SST gradient (figure not shown), and the rainfall anomalies are the result of ENSO-induced local effect. The weak bias of anticyclone at the south flank in SON(0) leads to weaker SST anomalies over the SIO in D(0)JF(1) (Figs. 1f, j, 17a). Moreover, due to the weaker

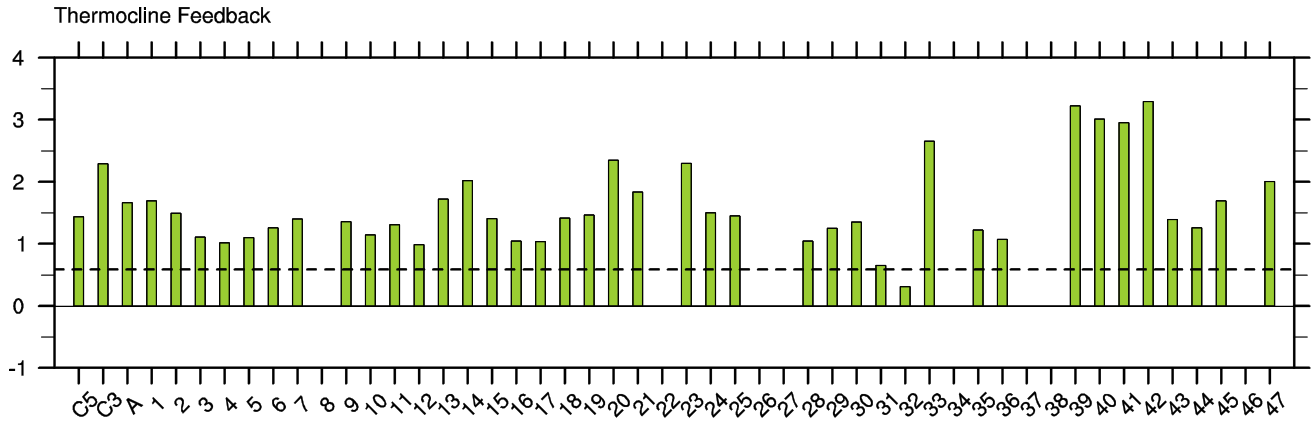

Fig. 14 As in Fig. 9, but for the thermocline feedback. The thermocline feedback index is the ratio between the SSH-induced SST anomalies and SSH change in Fig. 13

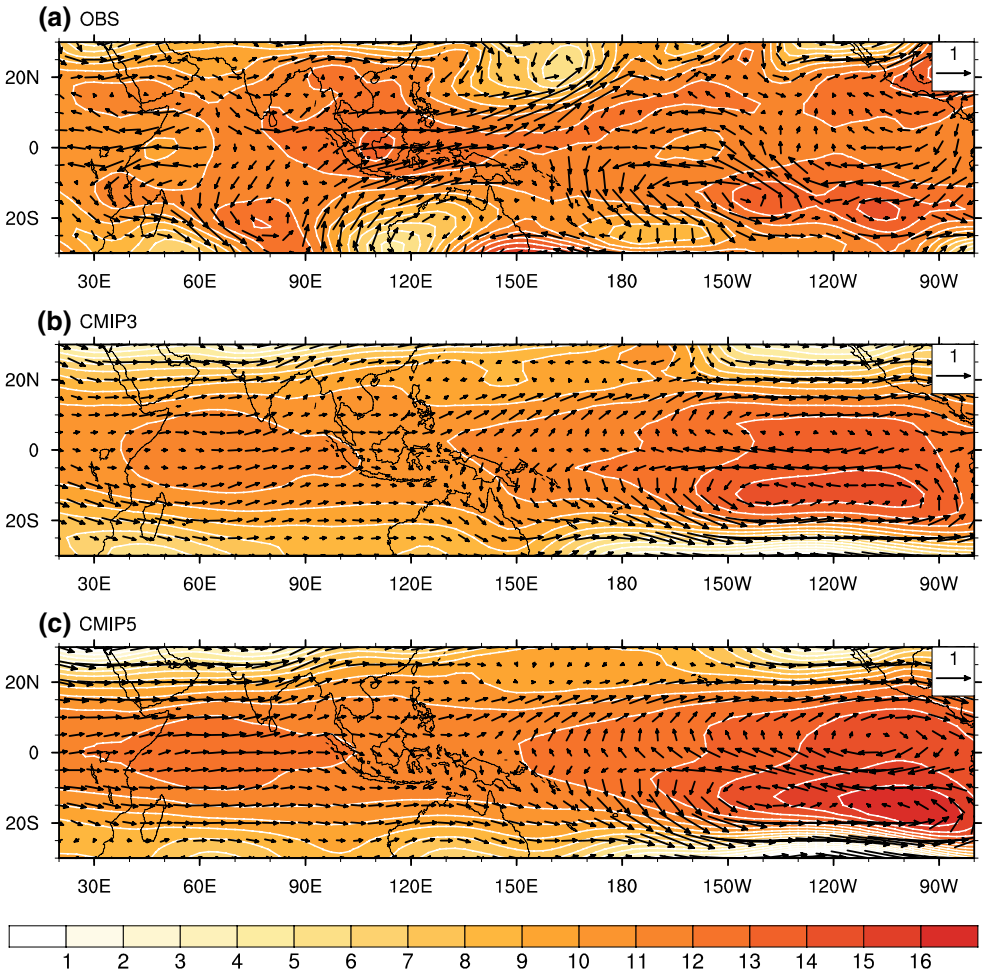

Fig. 15 Regression of 200 hPa geopotential height (*shaded*, gpm), 200 hPa wind (*vector*, ms^{-1}) with respect to D(0)JF(1) Niño3.4 index during JJA(1) for **a** observation, **b** CMIP3, and **c** CMIP5 MME

WES feedback (Fig. 9b), there is overall weak bias of LHF anomalies during the three seasons ("lh_num" in Figs. 8d–f, 17a–c). As mentioned before, the SWR anomalies are highly related to the precipitation anomalies over the TIO (Fig. 8a–c), and the CRS feedback is stronger in CMIP models (Fig. 9a). The suppressed

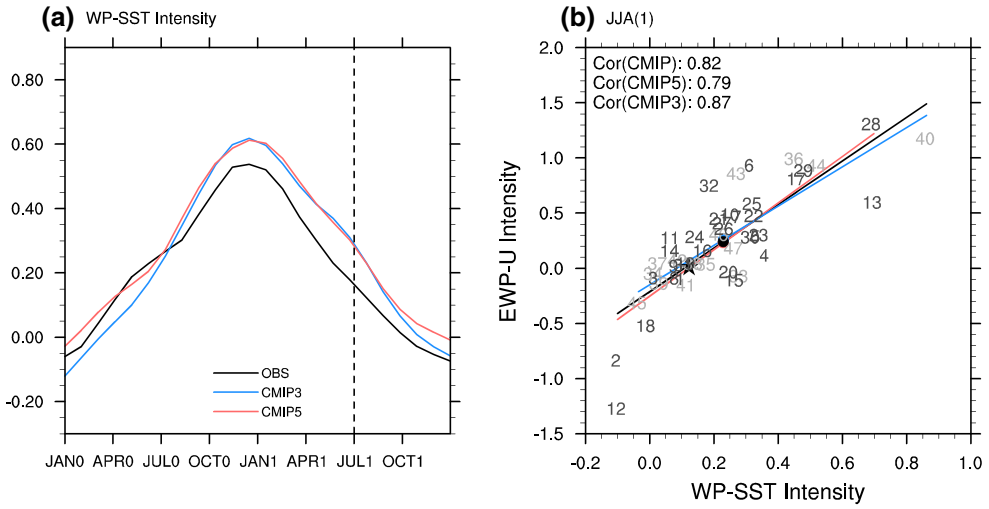

Fig. 16 **a** Regression of monthly SST anomalies over the equatorial WP (5°S–5°N, 150°E–150°W) with respect to D(0)JF(1) Niño3.4 index for observation (*black line*), CMIP3 (*blue line*) and CMIP5 (*red line*) MME. The *vertical dashed line* marks the JJA season when ENSO has dissipated in observation. **b** Scatter diagram of SST anomalies (abscissa) over the WP (5°S–5°N, 150°E–150°W) and zonal wind anomalies (ordinate) over equatorial WP (5°S–5°N, 150°E–180°) in JJA(1)

rainfall grid-numbers are comparable to the observation in SON(0) and MAM(1), and more in D(0)JF(1) due to the west bias of rainfall anomalies ("pr_num", in Fig. 17a–c). Thus, the overall downward SWR grid-numbers are slightly more in CMIP models ("sw_num", in Fig. 17a–c). The sum of SWR and LHF roughly constitutes NHF in the tropical oceans. There are less NHF grid-numbers in SON(0) and MAM(1) than observation due to reasonable SWR grid-numbers and less LHF grid-numbers, and more NHF grid-numbers in D(0)JF(1) due to more SWR grid-numbers and reasonable LHF grid-numbers ("nh_num", in Fig. 17a–c).

For the relationship between the SSH and SIO anticyclone as in Fig. 5, there exists west bias in SSH anomalies, which is associated with the west bias of anticyclone ("u_max_lon_SON" and "ssh_max_lon_SON", in Fig. 17a). As previous section, we focus on the DJF and MAM seasons. The simulated SWIO SSH anomalies are weaker than the observation ("ssh_index", in Fig. 17b, c). Though there is a deep bias of SWIO climatology thermocline ("clmssh_index", in Fig. 17b, c), the SSH-induced SST anomalies there are still comparable to the observation due to the stronger thermocline feedback ("reg_ssh_sst", in Fig. 17b, c).

Taking both atmospheric and oceanic processes into account, the less bias of downward NHF grid-numbers in SON(0) and weak bias of SSH-induced SST anomalies in D(0)JF(1) jointly cause slightly weak bias of D(0)JF(1) IOBM ("IOBM_DJF", in Fig. 17b). Due to more downward NHF grid-numbers in D(0)JF(1) and reasonable MAM(1) SSH-induced SST anomalies, the weak bias of MAM(1) IOBM is significantly reduced ("IOBM_MAM", in Fig. 17c). In JJA(1), the IOBM is slightly stronger than observation ("IOBM_JJA", in Fig. 17d), associated with the less downward NHF grid-numbers in MAM(1) and slightly stronger SSH-induced SST anomalies. This indicates that the effect of oceanic processes can persist into summer in CMIP models. Though there is reasonable IOBM simulation in JJA(1), the simulated of NWP anticyclone shows overall weak biases ("nwpac_index_JJA", in Fig. 17d), which is related to the unrealistic WP SST anomalies ("wpsst_JJA", in Fig. 17d).

Defining the average of these normalized biases as CMIP MME results, CMIP5 models show some improvement in the SON and MAM seasons, but no remarkable change in DJF and JJA compared with CMIP3 models (Fig. 17). To further investigate the performance of CMIP3 and CMIP5 models, we first calculate the STD of inter-model biases for each variable in CMIP3 and CMIP5 models respectively, and then the ratios of these CMIP5 and CMIP3 models. The results are shown in Fig. 18a. If the ratio is lower than one, the performance of CMIP5 models is better. Most variables, 26 out of 38 (about 70 %), show an improvement in CMIP5 models with a smaller spread of inter-model biases. On the other hand, Fig. 18b presents the STD of inter-variable biases for each model, and MME results of CMIP5 and CMIP3 models. The MME result of CMIP5 models has the smaller spread of inter-variable biases than CMIP3 models. In particular, some models show the excellent performance with smaller spread, as BCC-CSM1.1-M, GFDL-ESM2G, MIROC5 and so on. As a result, the overall performance of CMIP5 models is better than CMIP3 models, both on the MME and STD of biases.

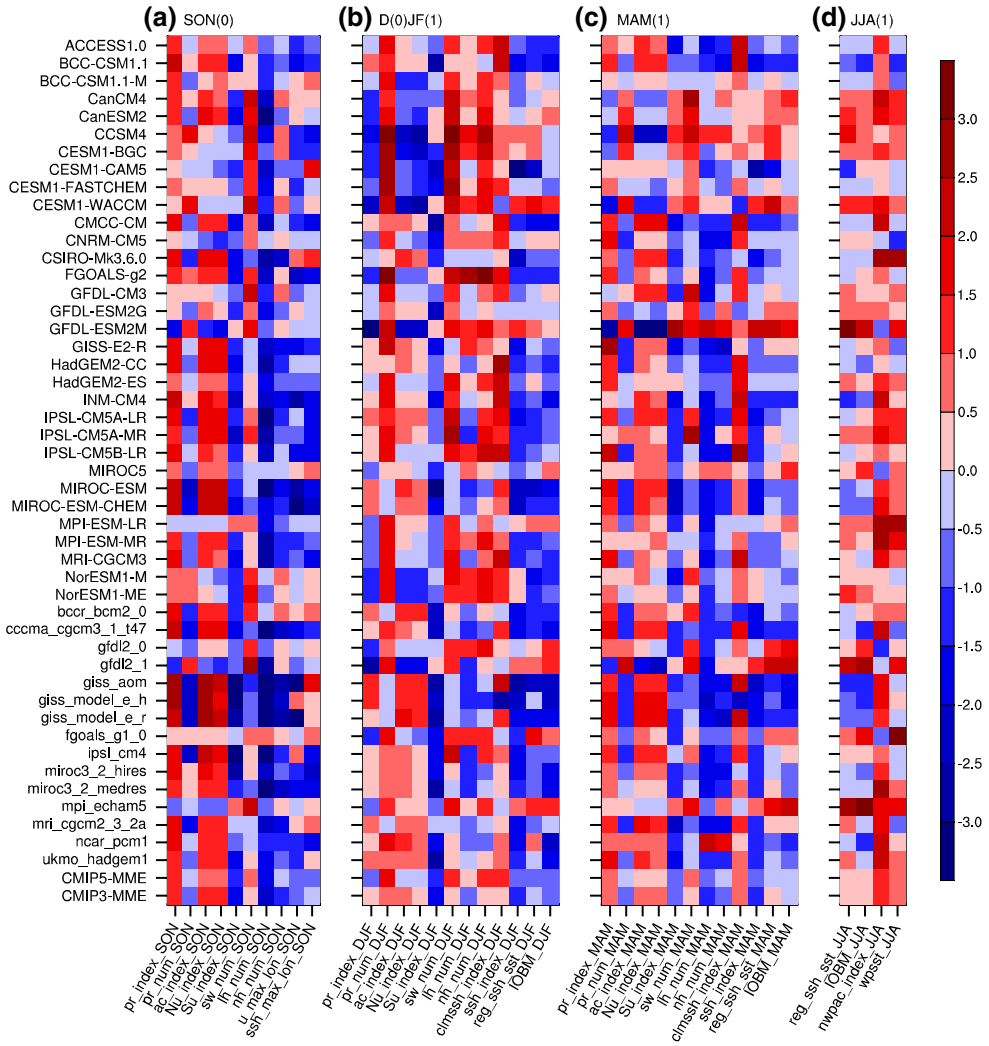

Fig. 17 The biases of each variable in IOBM for CMIP3 and CMIP5 models during **a** SON(0), **b** D(0)JF(1), **c** MAM(1), **d** JJA(1). "CMIP5-MME" and "CMIP3-MME" represent the MME of biases for each variable in CMIP3 and CMIP5 models respectively. The abscissa represents the variables in the evolution of IOBM, and each variable is introduced at the beginning of Sect. 5. The ordinate represents the names of CMIP models listed in Table 1

6 Summary

Based on the outputs of CMIP3 and CMIP5 models, this study has evaluated the biases of IOBM and its capacitor effect in 15 CMIP3 and 32 CMIP5 models. The main conclusions are summarized depending on the season and improvement from CMIP3 to CMIP5:

1. SON(0). The rainfall anomalies corresponding with SIO anticyclone extend overly westward compared to the observation, and the SSH anomalies also display a west bias. The suppressed rainfall anomalies over the MC and EIO display a weak bias, leading to a weak bias of SIO anticyclonic wind anomalies, especially along the south flank of the anticyclone. The simulated SSH anomalies are also weaker. Besides, the WES feedback is weaker in CMIP models. The weak bias in both anticyclone and feedback causes a weak bias of LHF simulation. The overall suppressed rainfall anomalies over the whole basin are slightly weaker than observation, and the CRS feedback is stronger in CMIP models, which, together, result in reasonable or slightly stronger SWR anomalies. The sum of SWR and LHF anomalies is weaker in the models, especially over the SIO, causing a weak bias of SST anomalies there in D(0)JF(1).
2. D(0)JF(1). There are slightly weaker SSH-induced SST anomalies in CMIP models due to the stronger thermocline feedback though there is a weak bias of ENSO-induced SSH anomalies. The overall effect of atmos-

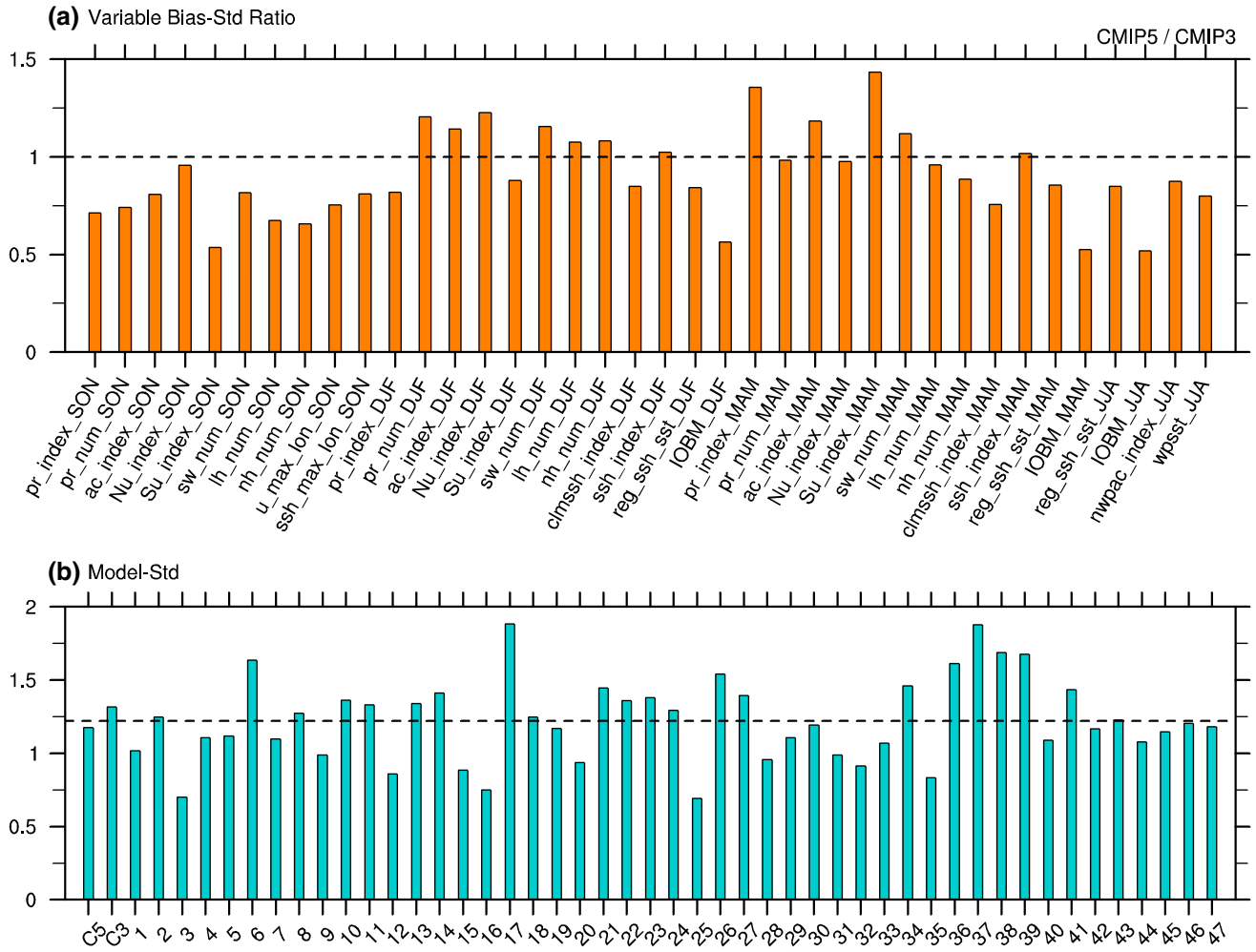

Fig. 18 **a** The ratios between the CMIP5 and CMIP3 standard deviations of inter-model biases for each variable. The *dashed lines* represent the ratio of one. **b** The standard deviations of inter-variable biases for each model (*number*), and MME results of CMIP5 ('C5') and CMIP3 ('C3') models. The *dashed lines* represent the result of all models MME

pheric and oceanic processes leads to a weak bias of IOBM simulation. The suppressed rainfall anomalies over the MC and EIO are comparable to or stronger than observation, owing to the west bias of precipitation anomalies which is possibly attributed to the west bias of simulated ENSO. As a result, the CMIP models simulate reasonable intensity of SIO anticyclone, but with a west bias. Due to a weaker WES feedback, the LHF anomalies are slightly weaker. Both stronger dry anomalies over the whole basin and strong bias of CRS feedback in CMIP models cause stronger SWR anomalies. The stronger SWR and slightly weaker LHF anomalies lead to stronger NHF anomalies in model simulations.

3. MAM(1). The SSH-induced SST anomalies in MAM(1) are comparable to observation, and NHF anomalies in D(0)JF(1) are stronger. Thus, the weak bias of IOBM simulation is significantly reduced in MAM(1). The weaker anticyclone is more likely due to weak bias of meridional SST gradient, resulting in weak bias of precipitation anomalies in MAM(1). The weaker wind anomalies and weaker WES feedback cause the weak bias of LHF anomalies, and weaker dry anomalies and stronger CRS feedback cause reasonable or slightly stronger SWR anomalies. Therefore, the NHF anomalies are slightly weaker in models.
4. JJA(1). In CMIP models, the effect of oceanic processes can persist into summer, offsetting the effect of slightly weaker NHF anomalies, so that the TIO warming lasts to summer. However, the NWP anticyclonic wind anomalies are weaker due to the weak and west bias of TIO capacitor effect. The unrealistic WP SST anomalies in CMIP models lead to a westward extension of Rossby wave with associated anomalous westerly winds from the Pacific, weakening anomalous easterly winds induced by the eastward Kelvin wave from

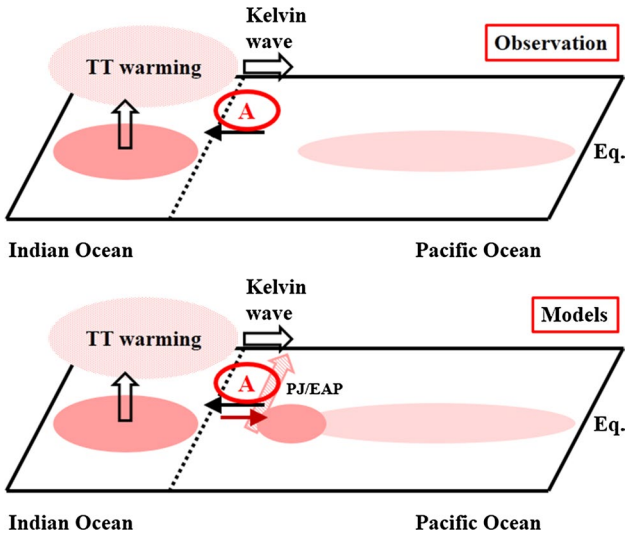

Fig. 19 Schematic diagram illustrating the mechanism of JJA(1) NWP anticyclone in observation (*top*) and models (*bottom*). *Pink shading* represents the SST anomalies. *Light pink* shading represents the dissipated SST anomalies of ENSO. *Black arrow* represents low level wind anomalies forced by Indian Ocean SST anomalies. *Dark red arrow* represents the low level wind anomalies forced by WP SST anomalies in models. *'A' in circle* represents the NWP anomalous anticyclone. The easterly wind anomalies are induced by the Kelvin wave response to TT warming over the Indian Ocean, forming the NWP anticyclone in observation. The WP unrealistic SST anomalies in models trigger the westward Rossby wave, forcing anomalous westerly winds, and weakening the easterly winds induced by the Kelvin wave. The WP warming forces the NWP anticyclone move farther north than observation, indicating the major forcing from the Pacific like the PJ/EAP teleconnection

the Indian Ocean. Moreover, the WP warming forces the NWP anticyclone move farther north (about 5°) than observation, suggesting the major forcing from the Pacific. The detailed mechanism is shown in Fig. 19.

5. Improvement from CMIP3 to CMIP5. For the feedback simulation, the CRS feedback in CMIP3 MME is weaker than observation, and stronger in CMIP5 MME. Thus, there seems no significant improvement in CRS feedback. However, though there are weak bias of WES feedback and strong bias of thermocline feedback, the CMIP5 MME simulates more realistic feedback than CMIP3. For the biases, CMIP5 models show some improvement in SON and MAM compared with CMIP3 models though there are no remarkable changes in DJF and JJA. The spread of inter-model biases also show improvement from CMIP3 to CMIP5. Thus, the overall performance of CMIP5 models is better than CMIP3 models.

The feedback bias may be originated from the model errors in association with the complex parameterization of physical processes. Leaving these feedback bias issues aside, the biases of IOBM simulation are ultimately related to the ENSO simulation. The problems about ENSO simulation in the state-of-the-art CGCMs still exist, including the intensity and westward extension of SST anomalies. The biases in SST anomalies are carried to rainfall simulation. The rainfall biases further affect the simulation of SIO anticyclone, and consequently the oceanic processes. Therefore, all these call for a breakthrough in CGCMs simulations of physical processes associated with ENSO.

Acknowledgments We acknowledge the World Climate Research Program's Working Group on Coupled Modeling, which is responsible for CMIP, and we thank the climate modeling groups (listed in Table 1 of this paper) for producing and making available their model output. For CMIP, the U.S. Department of Energy's Program for Climate Model Diagnosis and Intercomparison provides coordinating support and led development of software infrastructure in partnership with the Global Organization for Earth System Science Portals. We also thank two anonymous reviewers as well as the editor for their useful comments. This work was supported by the National Basic Research Program of China (2012CB955604 and 2011CB309704), the National Outstanding Youth Science Fund Project of China (41425019), and the National Natural Science Foundation of China (41205049, 41275083 and 91337105).

References

Alexander MA, Blade I, Newman M, Lanzante JR, Lau NC, Scott JD (2002) The atmospheric bridge: the influence of ENSO teleconnections on air-sea interaction over the global oceans. J Clim 15(16):2205–2231. doi:10.1175/1520-0442(2002)015<2205:tabtio>2.0.co;2

Bellenger H, Guilyardi E, Leloup J, Lengaigne M, Vialard J (2014) ENSO representation in climate models: from CMIP3 to CMIP5. Clim Dyn 42(7–8):1999–2018. doi:10.1007/s00382-013-1783-z

Cai W, Cowan T (2013) Why is the amplitude of the Indian Ocean Dipole overly large in CMIP3 and CMIP5 climate models? Geophys Res Lett 40(6):1200–1205. doi:10.1002/grl.50208

Carton JA, Giese BS (2008) A reanalysis of ocean climate using Simple Ocean Data Assimilation (SODA). Mon Weather Rev 136(8):2999–3017. doi:10.1175/2007mwr1978.1

Carton JA, Giese BS, Grodsky SA (2005) Sea level rise and the warming of the oceans in the Simple Ocean Data Assimilation (SODA) ocean reanalysis. J Geophys Res Oceans 110(C9):C09006. doi:10.1029/2004jc002817

Chen M, Xie P, Janowiak JE, Arkin PA (2002) Global land precipitation: a 50-yr monthly analysis based on gauge observations. J Hydrometeorol 3(3):249–266. doi:10.1175/1525-7541(2002)003<0249:glpaym>2.0.co;2

Chiang JCH, Lintner BR (2005) Mechanisms of remote tropical surface warming during El Nino. J Clim 18(20):4130–4149. doi:10.1175/jcli3529.1

Chiang JCH, Sobel AH (2002) Tropical tropospheric temperature variations caused by ENSO and their influence on the remote tropical climate. J Clim 15(18):2616–2631. doi:10.1175/1520-0442(2002)015<2616:tttvcb>2.0.co;2

Chowdary JS, Gnanaseelan C (2007) Basin-wide warming of the Indian Ocean during El Nino and Indian Ocean dipole years. Int J Climatol 27(11):1421–1438. doi:10.1002/joc.1482

Chowdary JS, Xie SP, Luo JJ, Hafner J, Behera S, Masumoto Y, Yamagata T (2011) Predictability of Northwest Pacific climate

during summer and the role of the tropical Indian Ocean. Clim Dyn 36(3–4):607–621. doi:10.1007/s00382-009-0686-5
Collins M, An SI, Cai WJ, Ganachaud A, Guilyardi E, Jin FF, Jochum M, Lengaigne M, Power S, Timmermann A, Vecchi G, Wittenberg A (2010) The impact of global warming on the tropical Pacific ocean and El Nino. Nat Geosci 3(6):391–397. doi:10.1038/ngeo868
Du Y, Xie SP, Huang G, Hu K (2009) Role of air–sea interaction in the long persistence of El Niño-induced north Indian Ocean warming. J Clim 22(8):2023–2038
Du Y, Yang L, Xie SP (2011) Tropical Indian Ocean influence on northwest Pacific tropical cyclones in summer following strong El Nino. J Clim 24(1):315–322. doi:10.1175/2010jcli3890.1
Du Y, Xie S-P, Yang Y-L, Zheng X-T, Liu L, Huang G (2013) Indian Ocean variability in the CMIP5 multimodel ensemble: the basin mode. J Clim 26(18):7240–7266. doi:10.1175/jcli-d-12-00678.1
Gill AE (1980) Some simple solutions for heat-induced tropical circulation. Q J R Meteorol Soc 106(449):447–462. doi:10.1256/smsqj.44904
Gong H, Wang L, Chen W, Wu R, Wei K, Cui X (2013) The climatology and interannual variability of the East Asian winter monsoon in CMIP5 models. J Clim 27(4):1659–1678. doi:10.1175/jcli-d-13-00039.1
Gong H, Wang L, Chen W, Nath D, Huang G, Tao W (2014) Diverse influences of ENSO on the East Asian-western Pacific winter climate tied to different ENSO properties in CMIP5 models. J Clim. doi:10.1175/jcli-d-14-00405.1
Ham Y-G, Kug J-S (2014) Improvement of ENSO simulation based on intermodel diversity. J Clim 28(3):998–1015. doi:10.1175/jcli-d-14-00376.1
Hu K, Huang G, Huang R (2011) The impact of tropical Indian Ocean variability on summer surface air temperature in China. J Clim 24(20):5365–5377
Hu K, Huang G, Qu X, Huang R (2012a) The impact of Indian Ocean variability on high temperature extremes across the southern Yangtze River valley in late summer. Adv Atmos Sci 29(1):91–100
Hu K, Huang G, Wu R (2012b) A strengthened influence of ENSO on August high temperature extremes over the Southern Yangtze River Valley since the late 1980s. J Clim 26(7):2205–2221. doi:10.1175/jcli-d-12-00277.1
Hu K, Huang G, Zheng X-T, Xie S-P, Qu X, Du Y, Liu L (2014) Interdecadal variations in ENSO influences on Northwest Pacific-East Asian early summertime climate simulated in CMIP5 models. J Clim 27(15):5982–5998. doi:10.1175/jcli-d-13-00268.1
Huang RH, Sun FY (1992) Impacts of the tropical western pacific on the East-Asian summer monsoon. J Meteorol Soc Jpn 70(1B):243–256
Huang G, Hu KM, Xie SP (2010) Strengthening of tropical Indian Ocean teleconnection to the Northwest Pacific since the Mid-1970s: an atmospheric GCM study. J Clim 23(19):5294–5304. doi:10.1175/2010jcli3577.1
Huang G, Qu X, Hu KM (2011) The impact of the tropical Indian Ocean on South Asian High in Boreal Summer. Adv Atmos Sci 28(2):421–432. doi:10.1007/s00376-010-9224-y
Huang P, Wang PF, Hu KM, Huang G, Zhang ZH, Liu Y, Yan BL (2014) An introduction to the integrated climate model of the Center for Monsoon System Research and Its Simulated Influence of El Nino on East Asian-Western North Pacific Climate. Adv Atmos Sci 31(5):1136–1146. doi:10.1007/s00376-014-3233-1
Kalnay E, Kanamitsu M, Kistler R, Collins W, Deaven D, Gandin L, Iredell M, Saha S, White G, Woollen J, Zhu Y, Chelliah M, Ebisuzaki W, Higgins W, Janowiak J, Mo KC, Ropelewski C, Wang J, Leetmaa A, Reynolds R, Jenne R, Joseph D (1996) The NCEP/NCAR 40-year reanalysis project. Bull Am Meteorol Soc 77(3):437–471. doi:10.1175/1520-0477(1996)077<0437:tnyrp>2.0.co;2
Kim ST, Yu JY (2012) The two types of ENSO in CMIP5 models. Geophys Res Lett 39:L11704. doi:10.1029/2012gl052006
Klein SA, Soden BJ, Lau N-C (1999) Remote sea surface temperature variations during ENSO: evidence for a tropical atmospheric bridge. J Clim 12(4):917–932. doi:10.1175/1520-0442(1999)012<0917:rsstvd>2.0.co;2
Lau NC, Nath MJ (1996) The role of the "Atmospheric Bridge" in linking tropical Pacific ENSO events to extratropical SST anomalies. J Clim 9:2036–2057
Lau NC, Nath MJ (2000) Impact of ENSO on the variability of the Asian–Australian monsoons as simulated in GCM experiments. J Clim 13(24):4287–4309. doi:10.1175/1520-0442(2000)013<4287:ioeotv>2.0.co;2
Lau NC, Nath MJ (2003) Atmosphere-ocean variations in the Indo-Pacific sector during ENSO episodes. J Clim 16(1):3–20. doi:10.1175/1520-0442(2003)016<0003:aoviti>2.0.co;2
Li G, Xie S-P, Du Y (2015a) Climate model errors over the South Indian Ocean thermocline dome and their effect on the basin mode of interannual variability. J Clim. doi:10.1175/jcli-d-14-00810.1
Li G, Xie S-P, Du Y (2015b) Monsoon-induced biases of climate models over the tropical Indian Ocean. J Clim. doi:10.1175/jcli-d-14-00740.1
Masumoto Y, Meyers G (1998) Forced Rossby waves in the southern tropical Indian Ocean. J Geophys Res Oceans 103(C12):27589–27602. doi:10.1029/98jc02546
Matsuno T (1966) Quasi-geostrophic motions in the equatorial area. J Meteor Soc Japan 44(1):25–43
Meehl GA, Covey C, Taylor KE, Delworth T, Stouffer RJ, Latif M, McAvaney B, Mitchell JFB (2007) THE WCRP CMIP3 multimodel dataset: a new era in climate change research. Bull Am Meteorol Soc 88(9):1383–1394. doi:10.1175/bams-88-9-1383
Murtugudde R, Busalacchi AJ (1999) Interannual variability of the dynamics and thermodynamics of the tropical Indian Ocean. J Clim 12(8):2300–2326. doi:10.1175/1520-0442(1999)012<2300:ivotda>2.0.co;2
Nitta T (1987) Convective activities in the tropical western Pacific and their impact on the Northern-Hemisphere summer circulation. J Meteorol Soc Jpn 65(3):373–390
Okumura YM, Deser C (2010) Asymmetry in the duration of El Niño and La Niña. J Clim 23(21):5826–5843. doi:10.1175/2010jcli3592.1
Qu X, Huang G (2012a) An enhanced influence of tropical Indian Ocean on the South Asia High after the late 1970s. J Clim 25(20):6930–6941. doi:10.1175/jcli-d-11-00696.1
Qu X, Huang G (2012b) Impacts of tropical Indian Ocean SST on the meridional displacement of East Asian jet in boreal summer. Int J Climatol 32(13):2073–2080. doi:10.1002/joc.2378
Ramanathan V, Collins W (1991) Thermodynamic regulation of ocean warming by cirrus clouds deduced from observations of the 1987 El Nino. Nature 351(6321):27–32
Rayner NA, Parker DE, Horton EB, Folland CK, Alexander LV, Rowell DP, Kent EC, Kaplan A (2003) Global analyses of sea surface temperature, sea ice, and night marine air temperature since the late nineteenth century. J Geophys Res Atmos 108(D14):4407. doi:10.1029/2002jd002670
Saji NH, Goswami BN, Vinayachandran PN, Yamagata T (1999) A dipole mode in the tropical Indian Ocean. Nature 401(6751):360–363. doi:10.1038/43855
Saji NH, Xie SP, Yamagata T (2006) Tropical Indian Ocean variability in the IPCC twentieth-century climate simulations. J Clim 19(17):4397–4417. doi:10.1175/jcli3847.1
Schott FA, Xie SP, McCreary JP (2009) Indian Ocean circulation and climate variability. Rev Geophys 47:RG1002. doi:10.1029/2007rg000245
Tao W, Huang G, Hu K, Qu X, Wen G, Gong Y (2014) Different influences of two types of El Niños on the Indian Ocean SST

variations. Theor Appl Climatol 117(3–4):475–484. doi:10.1007/s00704-013-1022-x

Tao W, Huang G, Hu K, Qu X, Wen G, Gong H (2015) Interdecadal modulation of ENSO teleconnections to the Indian Ocean Basin mode and their relationship under global warming in CMIP5 models. Int J Climatol 35(3):391–407. doi:10.1002/joc.3987

Taylor KE, Stouffer RJ, Meehl GA (2011) An overview of CMIP5 and the experiment design. Bull Am Meteorol Soc 93(4):485–498. doi:10.1175/bams-d-11-00094.1

Wang B, Xie X (1996) Low-frequency equatorial waves in vertically sheared zonal flow. Part I: stable waves. J Atmos Sci 53(3):449–467. doi:10.1175/1520-0469(1996)053<0449:lfewiv>2.0.co;2

Wang B, Wu R, Li T (2003) Atmosphere–warm Ocean interaction and its impacts on Asian–Australian monsoon variation. J Clim 16(8):1195–1211. doi:10.1175/1520-0442(2003)16<1195:aoiaii>2.0.co;2

Webster PJ, Moore AM, Loschnigg JP, Leben RR (1999) Coupled ocean–atmosphere dynamics in the Indian Ocean during 1997–98. Nature 401(6751):356–360. doi:10.1038/43848

Wu R, Yeh S-W (2010) A further study of the tropical Indian Ocean asymmetric mode in boreal spring. J Geophys Res Atmos 115(D8):D08101. doi:10.1029/2009jd012999

Wu R, Kirtman BP, Krishnamurthy V (2008) An asymmetric mode of tropical Indian Ocean rainfall variability in boreal spring. J Geophys Res Atmos 113(D5):D05104. doi:10.1029/2007jd009316

Xie SP, Philander SGH (1994) A coupled ocean-atmosphere model of relevance to the itcz in the eastern pacific. Tellus Ser A Dyn Meteorol Oceanol 46(4):340–350. doi:10.1034/j.1600-0870.1994.t01-1-00001.x

Xie X, Wang B (1996) Low-frequency equatorial waves in vertically sheared zonal flow. Part II: unstable waves. J Atmos Sci 53(23):3589–3605. doi:10.1175/1520-0469(1996)053<3589:lfewiv>2.0.co;2

Xie SP, Annamalai H, Schott FA, McCreary JP Jr (2002) Structure and mechanisms of south Indian Ocean climate variability. J Clim 15(8):864–878

Xie SP, Hu K, Hafner J, Tokinaga H, Du Y, Huang G, Sampe T (2009) Indian Ocean capacitor effect on Indo-western Pacific climate during the summer following El Niño. J Clim 22(3):730–747

Xie SP, Du Y, Huang G, Zheng XT, Tokinaga H, Hu KM, Liu QY (2010) Decadal shift in El Nino influences on Indo-Western Pacific and East Asian climate in the 1970s. J Clim 23(12):3352–3368. doi:10.1175/2010jcli3429.1

Yang J, Liu Q, Xie S, Liu Z, Wu L (2007) Impact of the Indian Ocean SST basin mode on the Asian summer monsoon. Geophys Res Lett 34(2):L02708. doi:10.1029/2006gl028571

Yang J, Liu Q, Liu Z, Wu L, Huang F (2009) Basin mode of Indian Ocean sea surface temperature and Northern Hemisphere circumglobal teleconnection. Geophys Res Lett 36(19):L19705. doi:10.1029/2009gl039559

Yang J, Liu Q, Liu Z (2010) Linking observations of the Asian monsoon to the Indian Ocean SST: possible roles of Indian Ocean basin mode and dipole mode. J Clim 23(21):5889–5902. doi:10.1175/2010jcli2962.1

Yu LS, Rienecker MM (1999) Mechanisms for the Indian Ocean warming during the 1997–98 El Nino. Geophys Res Lett 26(6):735–738. doi:10.1029/1999gl900072

Yulaeva E, Wallace JM (1994) Signature of enso in global temperature and precipitation fields derived from the microwave sounding unit. J Clim 7(11):1719–1736. doi:10.1175/1520-0442(1994)007<1719:tsoeig>2.0.co;2

Zhang T, Sun D-Z (2014) ENSO asymmetry in CMIP5 models. J Clim 27(11):4070–4093. doi:10.1175/jcli-d-13-00454.1

Zheng XT, Xie SP, Liu QY (2011) Response of the Indian Ocean basin mode and its capacitor effect to global warming. J Clim 24(23):6146–6164. doi:10.1175/2011jcli4169.1